



# Identification of material parameters and traction field for soft bodies in contact

T. Lavigne<sup>a</sup>, S.P.A. Bordas<sup>a,b,\*</sup>, J. Lengiewicz<sup>a,c</sup>

<sup>a</sup> *Department of Engineering; Faculty of Science, Technology and Medicine; University of Luxembourg, 6, avenue de la Fonte, Esch-sur-Alzette, L-4364, Luxembourg*

<sup>b</sup> *Visiting, Department of Medical Research, China Medical University Hospital, China Medical University, Taichung, Taiwan*

<sup>c</sup> *Institute of Fundamental Technological Research, Polish Academy of Sciences (IPPT PAN), Pawinskiego 5B, Warsaw, 02-106, Poland*

Received 2 August 2022; received in revised form 3 January 2023; accepted 4 January 2023

Available online xxxx

## Abstract

We provide an optimization framework that is capable of identifying the material parameters and contact traction field from two measured deformed geometries of a soft body in contact. The novelty of the framework is the idea of parametrizing the missing contact traction field and incorporating it into the inverse+forward hyper-elasticity formulation. We provide the continuum- and finite element formulation of the framework, as well as the direct differentiation method of sensitivity analysis to efficiently obtain necessary gradients for the BFGS optimizer. The correctness of the formulation and the excellent performance of the framework are confirmed by a series of benchmark numerical examples.

© 2023 Published by Elsevier B.V.

**Keywords:** Hyper-elasticity; Inverse form; Large strains; Contact; Calibration; Soft bodies

## 1. Introduction

In many practical applications, soft structures and tissues can only be observed in significantly deformed configurations. For instance, in the context of biomechanics, *in vivo* imaging techniques operate on tissues that are deformed at least under their weights [1,2]. In the case of breast cancer screening, the organ is additionally constrained by contacts with external devices [3–6] or self-contact [2]. In brain imaging, the leak of cerebrospinal fluid during the surgery leads to brain shift, i.e., the rigid motion of the brain in the skull combined with its consolidation under its weight [7]. For understanding abdominal aortic aneurysms, computing the residual stresses [8,9] or the open configuration [10] is a crucial step for obtaining accurate simulations.

This inherent inability to measure the unloaded (stress-free) configuration poses problems for modeling- and model calibration procedures. This is because we are focused on large-deformation models, which is a generalization to the standard model-based elastography that only calibrates apparent parameters around a given loaded state, see, e.g., Dooley [11]. To make it possible to calibrate large-deformation models, it is desirable to develop theoretical/computational modeling frameworks that could either assess the load-free configuration or directly operate on different loaded configurations.

\* Corresponding author.

E-mail address: [stephane.bordas@alumn.northwestern.edu](mailto:stephane.bordas@alumn.northwestern.edu) (S.P.A. Bordas).

Several techniques were established to assess the *load-free* configuration of a given measured *loaded* configuration. If the loading is known, the easiest is to reverse the direction of loading, see, e.g., Eiben et al. [12]. However, this method is only suitable in the small deformation regime and is in general inaccurate in the case of large deformations (soft bodies or in case of elasto-plasticity). In a more general case, one needs to solve an implicit problem of finding an unloaded configuration such that, after the application of the loading, the expected measured configuration is recovered. Within this general approach, several iterative schemes were proposed, see Eiben et al. [12,13], Carter et al. [14], Gee et al. [15], Weisbecker et al. [16] and Landkammer et al. [17]. Originally, the algorithm was introduced by Sellier [18] with a fixed-point method for elastostatic problems and then generalized to the backward displacement method by Bols [19] for patient-specific blood vessel simulations.

The iterative schemes only utilize forward simulations to iteratively converge to a desired unloaded configuration. Because of this, they can be used with practically any finite element solver. They are however computationally expensive because many iterations are required to converge a satisfying solution. To circumvent this efficiency issue, various direct inverse motion formulations were proposed, see, e.g., Govindjee and Mihalic [20], Mazier et al. [21] and Rajagopal et al. [22]. They are based on inverse kinematics, in which the deformed (current) configuration is known and the undeformed one corresponds to the primary unknowns. The goal is to solve the classical weak form of the equilibrium expressed in the current (loaded) configuration (i.e., based on the Eulerian description and the Cauchy stress tensor).

The direct inverse motion methodology to obtain unloaded configurations, and possibly use it as a part of the calibration procedure, is based on the assumption that both the geometry and the external forces are known in the given loaded configuration. This assumption cannot be that easily satisfied if the loaded configuration includes *contact*. The reason for that is that the necessary contact traction field is usually experimentally difficult to retrieve. This is particularly true for medical imaging of soft tissues, where contact or self-contact often occurs (Mira et al. [2,4] and Kuhlmann et al. [23]). In such situations of missing contact traction, the inverse elasticity problem cannot be solved.

This paper aims to tackle the inverse-elasticity-based identification problem with *contact*. (We limit ourselves to path-independent problems/models: hyperelasticity with frictionless contact.) To do so, we consider not one but two different deformed configurations, both of which can potentially include contact. We parametrize the missing contact traction field and solve a certain optimization problem to identify these parameters simultaneously together with material parameters. This poses a new identification problem, for which we additionally solve the sensitivity problem for the gradient-based optimization procedure. We demonstrate the performance of our framework on artificially (numerically) generated benchmark cases, with and without contact. In order to assess applicability of the framework to work with experimental data, we also analyze the influence of noise in data.

The proposed approach fits into a well-established class of full-field measurement based model calibration techniques, see, e.g., Avril et al. [24], Goenezen et al. [25], Pierron and Grédiac [26], Barbone et al. [27], Hild et al. [28], Pan [29], Pierron and Grédiac [30] and Borzeszkowski et al. [31]. The novelty of our approach is that we aim to identify contact tractions in addition to calibrating material parameters, and that we assume to only know loaded configurations. The present approach resembles some of the problems of shape optimization with contact, see, e.g., Stupkiewicz et al. [32], Beremlijski et al. [33] and Hilding et al. [34], as in both cases the unloaded shape undergoes changes upon optimization. However, in the present case, this is the contact traction field being parametrized, not directly the geometry. Even more distinctive, the present approach involves not two but three configurations, with subsequent inverse and forward elasticity problems to be solved in between. A similar direction to what we propose has been recently taken in Song et al. [35] to develop a calibration framework in cell biomechanics. Similarly to us, they parametrize the traction field to be part of the calibration procedure that is done through the inverse elasticity formulation. However, there are several important differences. The first difference is that in Song et al. [35] they assume to have a direct access to the unloaded configuration, while in our case only fully loaded configurations are considered. The second difference is that they do not explicitly consider contact interactions, which in our case are possible in both loaded configurations. The third difference is that they calibrate traction vectors individually per node, while in our case the number of parameters determining the unknown traction field can be more precisely controlled, which may allow for reduction of computational costs and can have a regularizing effect on the identification procedure.

The organization of the paper is the following. In Section 2 we shortly introduce the forward and inverse (hyper-)elasticity problem with contact. Then, in Section 3, we introduce the identification framework: first only

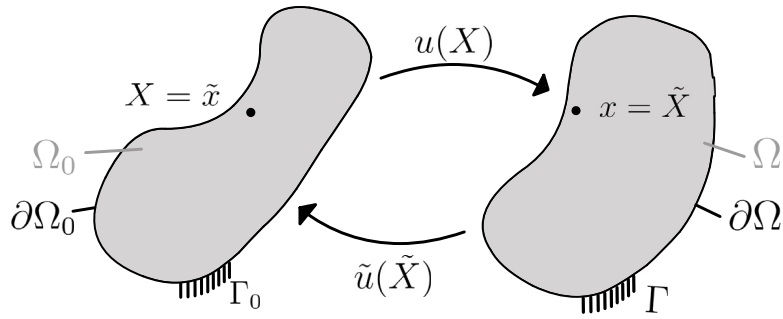


Fig. 1. Kinematic variables for the forward and inverse elasticity problems.

for the contact-less case and afterward for the case including contact. In Section 4 we provide three benchmark problems that demonstrate the concept and quantitatively assess the efficiency of the method. The paper is concluded in Section 5.

## 2. Forward and inverse elasticity formulations

### 2.1. Forward hyper-elasticity

We will shortly introduce a standard quasi-static hyper-elasticity formulation. The strong form of the equilibrium equations reads

$$\nabla_{\mathbf{X}} \cdot \mathbf{P} + \rho_0 \mathbf{b} = \mathbf{0} \tag{1}$$

which is accompanied by an appropriate constitutive relationship between the stress and strain measures through a hyper-elastic potential  $W(\mathbf{F})$

$$\mathbf{P} = \frac{\partial W}{\partial \mathbf{F}}. \tag{2}$$

In the equations above,  $\mathbf{P} = J \boldsymbol{\sigma} \mathbf{F}^{-T}$  is the first Piola–Kirchhoff stress tensor defined in terms of the Cauchy stress tensor  $\boldsymbol{\sigma}$ ,  $\rho_0$  is the density of the material,  $\mathbf{b}$  are body forces and

$$\mathbf{F}(\mathbf{X}) = \mathbf{I} + \nabla_{\mathbf{X}} \mathbf{u} \tag{3}$$

is the deformation gradient with its determinant  $J = \det(\mathbf{F})$ , see also Fig. 1. We use the notation  $\nabla_{\mathbf{X}}$  to denote gradients with respect to the reference configuration  $\mathbf{X} \in \Omega_0$ .

We specify here a particular form of the hyper-elastic strain energy potential (Neo-Hookean), see Simo and Taylor [36],

$$W(\mathbf{F}) = \frac{\mu}{2} (\text{Tr}(\mathbf{F}^T \mathbf{F}) - 3 - 2 \log(J)) + \frac{\lambda}{4} (J^2 - 1 - 2 \log(J)), \tag{4}$$

where the Lamé constants  $\mu = \frac{E}{2(1-\nu)}$  and  $\lambda = \frac{E\nu}{(1+\nu)(1-2\nu)}$  are material parameters expressed in term of the Young’s modulus,  $E$ , and Poisson ratio,  $\nu$  (see also Doll and Schweizerhof [37] for other forms of the volumetric part of the potential). This model will be used in the examples provided in Section 4. Note, however, that in principle, by replacing the strain energy potential, any other hyper-elastic model can be used within the proposed framework, including the Mooney–Rivlin model, and a more general class of Ogden models, see Ogden [38].

The associated weak form, suitable for the finite element formulation, is obtained by multiplying the strong form by the kinematically admissible test functions  $\delta \mathbf{v}(\mathbf{X})$

$$\int_{\Omega_0} (\nabla_{\mathbf{X}} \cdot \mathbf{P}) \cdot \delta \mathbf{v} \, d\Omega_0 + \int_{\Omega_0} (\rho_0 \mathbf{b}) \cdot \delta \mathbf{v} \, d\Omega_0 = 0. \tag{5}$$

This is then transformed (Green–Ostrogradski theorem) to

$$\int_{\Omega_0} \mathbf{P} : \nabla_{\mathbf{X}} \delta \mathbf{v} \, d\Omega_0 - \int_{\Omega_0} (\rho_0 \mathbf{b}) \cdot \delta \mathbf{v} \, d\Omega_0 - \int_{\Gamma_0^t} \mathbf{t}_0 \cdot \delta \mathbf{v} \, d\Gamma_0^t = 0, \tag{6}$$

in which the Neumann boundary conditions are recovered by applying (nominal) traction  $\mathbf{t}_0$  at the boundary  $\Gamma_0^t = \partial\Omega_0/\Gamma_0^u$ . The problem, in the weak form, is to find the displacement field  $\mathbf{u}(\mathbf{X})$  such that Eq. (6) holds for any kinematically admissible test functions  $\delta\mathbf{v}(\mathbf{X})$ .

The contact constraints in the (forward) hyper-elasticity formulation can be introduced in various ways, see e.g., Laursen [39], Wriggers [40] and Lengiewicz et al. [41]. In the present paper, we only consider simple frictionless contact with flat rigid obstacles, and we follow the standard penalty formulation, that can be found in Lengiewicz et al. [41]. The corresponding weak form that includes contact constraints reads

$$\int_{\Omega_0} \mathbf{P} : \nabla_{\mathbf{X}} \delta\mathbf{v} - \rho_0 \mathbf{b} \cdot \delta\mathbf{v} \, d\Omega_0 - \int_{\Gamma_0^t} \mathbf{t}_0 \cdot \delta\mathbf{v} \, d\Gamma_0^t - \int_{\Gamma_0^c} t_N \mathbf{n} \cdot \delta\mathbf{v} \, d\Gamma_0^c = 0, \tag{7}$$

where  $\Gamma_0^c$  is the boundary of potential contact,  $\mathbf{n}$  is the normal to the obstacle’s surface (at the point of orthogonal projection), and

$$t_N = \begin{cases} -\epsilon_c g_N & \text{if } g_N \leq 0 \text{ (contact)} \\ 0 & \text{if } g_N > 0 \text{ (separation)} \end{cases} \tag{8}$$

is the Penalty regularization of contact constraint, in which  $g_N$  is the normal gap and  $\epsilon_c > 0$  is the regularization parameter.

### 2.2. Direct inverse hyper-elasticity

The problem of inverse hyper-elasticity can be expressed in terms of the already introduced forward elasticity problem, see Section 2.1. Specifically, having a given loaded configuration, the goal is to find an unloaded configuration such that the loaded configuration will be the solution to the forward elasticity problem. The fundamental difference with respect to the forward elasticity problem is that, in the present case, the unloaded configuration  $\Omega_0$  is *unknown* while the loaded configuration  $\Omega$  is *known*, see also Fig. 1. The body forces and Neumann boundary conditions are assumed to be known. The problem is to find the inverse deformation field  $\tilde{\mathbf{u}}(\tilde{\mathbf{X}})$ , which corresponds to the solution  $\mathbf{u}(\mathbf{X})$  of the forward elasticity problem given by Eqs. (2) and (6) through

$$\tilde{\mathbf{u}} = -\mathbf{u}(\tilde{\mathbf{u}} + \tilde{\mathbf{X}}). \tag{9}$$

The proposed approach, borrowed from Govindjee and Mihalic [20] and Mazier et al. [21], relies on solving the same form of equilibrium as in Eq. (6) but for different variables, a different integration space, and a different definition of the gradients.

Let us consider the notation as in Fig. 1, in which  $\mathbf{X}(\tilde{\mathbf{X}}) = \tilde{\mathbf{X}} + \tilde{\mathbf{u}}$  and  $\mathbf{x}(\tilde{\mathbf{X}}) = \tilde{\mathbf{X}}$ . The (forward) deformation gradient can be then expressed as:

$$\mathbf{F}(\tilde{\mathbf{X}}) = \frac{d\mathbf{x}}{d\mathbf{X}} = \left( \frac{d\mathbf{X}}{d\mathbf{x}} \right)^{-1} = (\mathbf{I} + \nabla_{\tilde{\mathbf{X}}} \tilde{\mathbf{u}})^{-1}. \tag{10}$$

Importantly, this is a new definition of  $\mathbf{F}$  as compared to Eq. (3). All quantities derived from  $\mathbf{F}(\tilde{\mathbf{X}})$  depend on  $\tilde{\mathbf{u}}$  and are defined on the (fixed) domain  $\Omega$ . For that reason, a more suitable weak form that corresponds to Eq. (6) reads

$$\int_{\Omega} \left( \boldsymbol{\sigma} : \nabla_{\tilde{\mathbf{X}}} \delta\tilde{\mathbf{v}} - \frac{1}{J} \rho_0 \mathbf{b} \cdot \delta\tilde{\mathbf{v}} \right) d\Omega - \int_{\Gamma^t} \mathbf{t} \cdot \delta\tilde{\mathbf{v}} \, d\Gamma^t = 0. \tag{11}$$

Here

$$\boldsymbol{\sigma} = \frac{1}{J} \mathbf{P} \mathbf{F}^T, \tag{12}$$

and  $\mathbf{P}$  is obtained from the same elastic energy potential as in the forward problem, see Eq. (2), while  $J = \det(\mathbf{F}(\tilde{\mathbf{X}}))$ , and  $\delta\tilde{\mathbf{v}} = \delta\tilde{\mathbf{v}}(\tilde{\mathbf{X}})$  is a kinematically admissible trial function. Note that

$$\mathbf{t} = \frac{1}{J} \mathbf{t}_0 \mathbf{F}^T \tag{13}$$

includes  $\mathbf{t}_0$  that is assumed to be known.

If the known loaded configuration includes contact, the respective weak form reads

$$\int_{\Omega} \left( \boldsymbol{\sigma} : \nabla_{\bar{\mathbf{X}}} \delta \tilde{\mathbf{v}} - \frac{1}{J} \rho_0 \mathbf{b} \cdot \delta \tilde{\mathbf{v}} \right) d\Omega - \int_{\Gamma^t} \mathbf{t} \cdot \delta \tilde{\mathbf{v}} d\Gamma^t - \int_{\Gamma^c} \mathbf{t}_c \cdot \delta \tilde{\mathbf{v}} d\Gamma^c = 0, \tag{14}$$

and involves the contact traction field  $\mathbf{t}_c$ . In many practical cases, this traction field is unknown. Quite obviously, if  $\mathbf{t}_c$  is chosen improperly then the computed unloaded configuration is incorrect (this is demonstrated in the example shown in Fig. 14 in Section 4.3). As a solution to this problem, in Section 3.2 we will provide an identification framework to assess this unknown contact traction field.

### 2.3. Finite element formulation

The finite element formulation of the forward elasticity problems with contact, as defined in Eq. (7), is standard, see for instance Laursen [39], Wriggers [40] and Lengiewicz et al. [41]. The FE formulation of the inverse elasticity problem is analogous. For the sake of completeness, below, we will briefly introduce them both.

For the forward elasticity problem, we will work with the weak form defined by Eq. (7). After FE discretization, we will use its isoparametric form, in which the positions  $\mathbf{X} \in \Omega_0$  are transformed to local coordinates  $\boldsymbol{\Xi} \in \square$ . For a corresponding finite element, the discretized quantities at an integration point  $\boldsymbol{\Xi}$  read

$$\mathbf{X}(\boldsymbol{\Xi}) = \sum_{i=1}^n \mathbb{N}_i(\boldsymbol{\Xi}) \mathbb{X}_i, \quad \mathbf{u}(\boldsymbol{\Xi}) = \sum_{i=1}^n \mathbb{N}_i(\boldsymbol{\Xi}) \mathfrak{u}_i, \tag{15}$$

$$\mathbf{t}_0(\boldsymbol{\Xi}) = \sum_{i=1}^n \mathbb{N}_i(\boldsymbol{\Xi}) \mathfrak{t}_{0,i}, \quad \mathbf{t}_N(\boldsymbol{\Xi}) = \sum_{i=1}^n \mathbb{N}_i(\boldsymbol{\Xi}) \mathfrak{t}_{N,i}, \tag{16}$$

where  $n$  refers to the number of nodes in a given finite element, and  $\mathbb{N}_i$  are the associated shape functions. The double-stroke variables are the vectors of nodal values (possibly multi-dimensional), for which the index  $i$  refers to the local indexing in a given element. The displacement gradient and the Jacobian of the isoparametric transformation read

$$\nabla_{\mathbf{X}} \mathbf{u} = \frac{d\mathbf{u}}{d\boldsymbol{\Xi}} \left( \frac{d\mathbf{X}}{d\boldsymbol{\Xi}} \right)^{-1}, \quad J_{\boldsymbol{\Xi}} = \det \left( \frac{d\mathbf{X}}{d\boldsymbol{\Xi}} \right). \tag{17}$$

When using the Bubnov–Galerkin method, we set

$$\delta \mathbf{v} = \frac{d\mathbf{u}}{d\mathfrak{u}}, \quad \text{and} \quad \nabla_{\mathbf{X}} \delta \mathbf{v} = \frac{d\nabla_{\mathbf{X}} \mathbf{u}}{d\mathfrak{u}}. \tag{18}$$

With the definitions introduced above, together with Eqs. (2)–(4) and (8), after applying chosen numerical quadratures, we can transform the weak form of Eq. (7) into the balance equations in the residual form:

$$\mathbb{R}(\mathfrak{u}; \mathbb{X}) \equiv \mathbb{R}_v + \mathbb{R}_t + \mathbb{R}_c = \mathbf{0}, \tag{19}$$

where

$$\mathbb{R}_v = \mathbf{A}_{k \in \mathcal{E}_v} \left[ \sum_{i \in \mathcal{G}^k} w^{k,i} J_{\boldsymbol{\Xi}}^{k,i} \cdot \left( \boldsymbol{\sigma}^{k,i} : \nabla_{\mathbf{X}} \delta \mathbf{v}^{k,i} - \rho_0 \mathbf{b}^{k,i} \cdot \delta \mathbf{v}^{k,i} \right) \right], \tag{20}$$

$$\mathbb{R}_t = -\mathbf{A}_{k \in \mathcal{E}_t} \left[ \sum_{i \in \mathcal{G}^k} w^{k,i} J_{\boldsymbol{\Xi}}^{k,i} \cdot \left( \mathbf{t}^{k,i} \cdot \delta \mathbf{v}^{k,i} \right) \right], \tag{21}$$

$$\mathbb{R}_c = -\mathbf{A}_{k \in \mathcal{E}_c} \left[ \sum_{i \in \mathcal{G}^k} w^{k,i} J_{\boldsymbol{\Xi}}^{k,i} \cdot \left( \mathbf{t}_N^{k,i} \mathbf{n}^{k,i} \cdot \delta \mathbf{v}^{k,i} \right) \right]. \tag{22}$$

Above,  $\mathbf{A}$  stands for the FE assembly operator over the set of elements  $\mathcal{E}$ , while  $\mathcal{G}^k$  and  $w^{k,i}$  are the set of element integration points and their weights, respectively. Given an initial configuration  $\mathbb{X}$ , the set of non-linear Eqs. (19) can be solved for the unknown vector  $\mathfrak{u}$ .

For the inverse elasticity problem, the FE discretization takes a form that is analogous to the forward-elasticity version (Eqs. (15)–(18)):

$$\tilde{\mathbf{X}}(\boldsymbol{\varepsilon}) = \sum_{i=1}^n \mathbb{N}_i(\boldsymbol{\varepsilon}) \tilde{\mathbf{X}}_i, \quad \tilde{\mathbf{u}}(\boldsymbol{\varepsilon}) = \sum_{i=1}^n \mathbb{N}_i(\boldsymbol{\varepsilon}) \tilde{\mathbf{u}}_i, \quad (23)$$

$$\mathbf{t}_0(\boldsymbol{\varepsilon}) = \sum_{i=1}^n \mathbb{N}_i(\boldsymbol{\varepsilon}) \mathbf{t}_{0,i}, \quad \mathbf{t}_c(\boldsymbol{\varepsilon}) = \sum_{i=1}^n \mathbb{N}_i(\boldsymbol{\varepsilon}) \mathbf{t}_{c,i}, \quad (24)$$

$$\nabla_{\tilde{\mathbf{X}}} \tilde{\mathbf{u}} = \frac{d\tilde{\mathbf{u}}}{d\boldsymbol{\varepsilon}} \left( \frac{d\tilde{\mathbf{X}}}{d\boldsymbol{\varepsilon}} \right)^{-1}, \quad \tilde{J}_{\boldsymbol{\varepsilon}} = \det \left( \frac{d\tilde{\mathbf{X}}}{d\boldsymbol{\varepsilon}} \right), \quad (25)$$

$$\delta \tilde{\mathbf{v}} = \frac{d\tilde{\mathbf{u}}}{d\tilde{\mathbf{u}}}, \quad \nabla_{\tilde{\mathbf{X}}} \delta \tilde{\mathbf{v}} = \frac{d\nabla_{\tilde{\mathbf{X}}} \tilde{\mathbf{u}}}{d\tilde{\mathbf{u}}}. \quad (26)$$

The residual form of the balance equations is based on the weak form given by Eq. (14), together with Eqs. (10), (12) and (13), and the constitutive relationship given by Eqs. (2) and (4). Similarly to Eq. (19), we write

$$\tilde{\mathbb{R}}(\tilde{\mathbf{u}}; \tilde{\mathbf{X}}) \equiv \tilde{\mathbb{R}}_v + \tilde{\mathbb{R}}_t + \tilde{\mathbb{R}}_c = \mathbf{0}, \quad (27)$$

where

$$\tilde{\mathbb{R}}_v = \mathbf{A}_{k \in \mathcal{E}_v} \left[ \sum_{i \in \mathcal{G}^k} w^{k,i} \tilde{J}_{\boldsymbol{\varepsilon}}^{k,i} \cdot \left( \boldsymbol{\sigma}^{k,i} : \nabla_{\tilde{\mathbf{X}}} \delta \tilde{\mathbf{v}}^{k,i} - \frac{1}{J} \rho_0 \mathbf{b}^{k,i} \cdot \delta \tilde{\mathbf{v}}^{k,i} \right) \right], \quad (28)$$

$$\tilde{\mathbb{R}}_t = -\mathbf{A}_{k \in \mathcal{E}_t} \left[ \sum_{i \in \mathcal{G}^k} w^{k,i} \tilde{J}_{\boldsymbol{\varepsilon}}^{k,i} \cdot \left( \mathbf{t}^{k,i} \cdot \delta \tilde{\mathbf{v}}^{k,i} \right) \right], \quad (29)$$

$$\tilde{\mathbb{R}}_c = -\mathbf{A}_{k \in \mathcal{E}_c} \left[ \sum_{i \in \mathcal{G}^k} w^{k,i} \tilde{J}_{\boldsymbol{\varepsilon}}^{k,i} \cdot \left( \mathbf{t}_c^{k,i} \cdot \delta \tilde{\mathbf{v}}^{k,i} \right) \right]. \quad (30)$$

Given an initial configuration  $\tilde{\mathbf{X}}$ , the set of non-linear Eqs. (27) can be solved for the unknown vector  $\tilde{\mathbf{u}}$ .

### 3. Inverse-elasticity-based identification framework

We will consider an identification problem involving two different (measured) configurations of the same body. The configurations originate from two different external loadings, that are known. As mentioned earlier, the assumption of only having deformed configurations is motivated by the experimental reality when dealing with soft bodies.

We expect the configurations to be provided in the form of an already discretized deformation field (FE mesh of nodal displacements between the loaded configurations). In the benchmark cases considered in this paper, the required displacement fields are naturally available because the known loaded configurations are generated from the same discretized unloaded configuration. The same is also possible in real-life applications where scans of a deformed body (e.g., MRI- or CT-scans) are provided. In this real-life case, the necessary discretized displacement fields can be obtained by applying the image segmentation of the scans with subsequent meshing, which are then combined with the digital image/volume correlation procedure, see, e.g., Buljac et al. [42], Auger et al. [43] and Lavigne et al. [44].

Our primary interest is in identifying the material parameters of an assumed material model of the body. In Section 3.1, we introduce the framework for the contactless case. For the case involving contact, the identification of the contact traction field will need to be also included in the optimization procedure, which will be provided in Section 3.2. In Section 3.3 we will introduce the pipeline for the direct differentiation method of sensitivity analysis to compute implicit gradients that are required by gradient-based identification procedures.

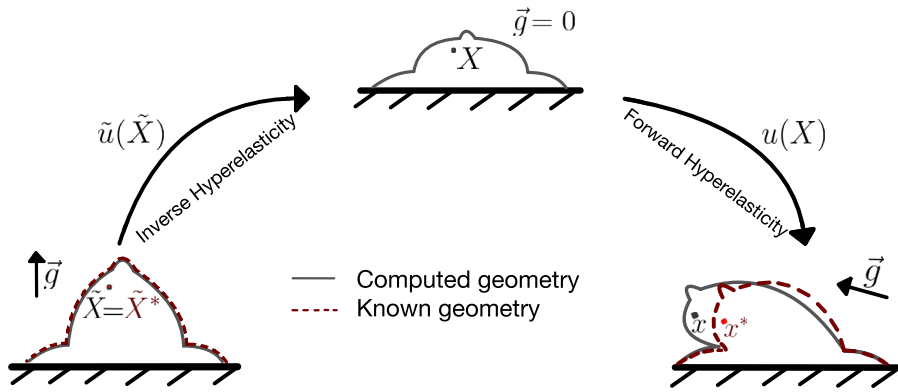


**Fig. 2.** Schematics of the inverse-forward problem used in the identification procedure. The reference configuration (left) is virtually unloaded (center) by solving the inverse hyper-elasticity problem and then loaded (right) by solving the classical forward hyper-elasticity problem. The desired known geometry is denoted by dashed lines.

### 3.1. Two deformed configurations — no contact

Knowing two loaded configurations and the loading conditions, the aim is to identify the material parameters,  $\phi$ , of the assumed material model of the body under consideration. The procedure is schematically shown in Fig. 2. It involves the known mapping  $\mathbf{x}^*(\tilde{\mathbf{X}}^*)$  between the two loaded configurations and the (trial) solution

$$\mathbf{x}(\tilde{\mathbf{X}}; \phi) = \mathbf{X} + \mathbf{u}(\mathbf{X}; \phi), \tag{31}$$

which incorporates the inverse elasticity part

$$\mathbf{X} = \mathbf{X}(\tilde{\mathbf{X}}; \phi) = \tilde{\mathbf{X}} + \tilde{\mathbf{u}}(\tilde{\mathbf{X}}; \phi). \tag{32}$$

In the expressions above,  $\tilde{\mathbf{u}}(\tilde{\mathbf{X}}; \phi)$  is the solution to the inverse elasticity problem,  $\tilde{\mathbb{R}}(\tilde{\mathbf{u}}; \phi) = \mathbf{0}$ , without contact, i.e., for  $\mathbf{t}_c = \mathbf{0}$ . This solution is then used to provide the initial configuration,  $\mathbf{X}(\phi)$ , for the forward elasticity problem,  $\mathbb{R}(\mathbf{u}; \phi) = \mathbf{0}$ , which is then solved to obtain  $\mathbf{u}(\mathbf{X}; \phi)$ .

The identification relies on finding a vector of material parameters  $\phi^*$  that brings the solution  $\mathbf{x}(\tilde{\mathbf{X}}; \phi^*)$  as close as possible to the desired solution  $\mathbf{x}^*(\tilde{\mathbf{X}})$ . (Note that  $\tilde{\mathbf{X}} = \tilde{\mathbf{X}}^*$  by definition.) This can be expressed in the form of minimization of the square error functional (the objective functional):

$$\phi^* = \underset{\phi}{\operatorname{argmin}} f(\phi) = \underset{\phi}{\operatorname{argmin}} \sum_{i \in \text{nodes}} (\mathbf{x}_i(\phi) - \mathbf{x}_i^*)^2. \tag{33}$$

In this work, the minimization is performed with the gradient-based method BFGS, see Nocedal and Wright [45]. The necessary gradient of the objective functional is expressed as:

$$\nabla_{\phi} f(\phi) = 2 \sum_{i \in \text{nodes}} \nabla_{\phi} \mathbf{x}_i \cdot (\mathbf{x}_i - \mathbf{x}_i^*), \tag{34}$$

where

$$\nabla_{\phi} \mathbf{x}_i = \nabla_{\phi} \tilde{\mathbf{X}}_i + \nabla_{\phi} \tilde{\mathbf{u}}(\tilde{\mathbf{X}}_i) + \nabla_{\phi} \mathbf{u}(\mathbf{X}_i). \tag{35}$$

Because the initial shape does not depend on  $\phi$ , the term  $\nabla_{\phi} \tilde{\mathbf{X}}_i$  vanishes. The remaining gradients in Eq. (35) can be computed by using the direct differentiation method of sensitivity analysis, which will be outlined in Section 3.3.

### 3.2. Two deformed configurations — with contact

When contact is present in the initial configuration for the inverse elasticity problem, the residual form given by Eq. (27) includes a non-vanishing *unknown* contact term  $\tilde{\mathbb{R}}_c$  given by Eq. (30). This makes it impossible to

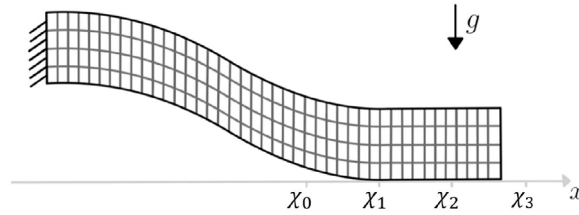


Fig. 3. Schematic of a contact region and four knot points  $\chi_i$  covering that region ( $n_x = 2$  case is present).

directly solve Eq. (27). The unique idea proposed in the present work is to parametrize the missing contact traction field:

$$t_c = t_c(\tilde{X}; \phi_c), \tag{36}$$

so that for a given vector of parameters  $\phi_c$ , the vector field  $t_c(\tilde{X}; \phi_c)$  is known over the potential contact boundary. These additional parameters can be then merged with the material parameters,  $\phi = \phi_c \cup \phi_m$ , and undergo the identification procedure expressed by Eq. (33).

To demonstrate the idea, below we will provide one of such parametrizations (which will be used in the example in Section 4.3). For the sake of clarity, we will restrict ourselves to a simple case in which a single-connected, horizontally-oriented, flat contact zone is present, see Fig. 3. Also, only the normal component of the traction field,  $t_N$ , will be considered (frictionless contact).

The construction of parametrization will be based on degree-one B-Splines, with a B-Spline basis

$$B^i(x, \chi) = \begin{cases} \frac{x - \chi_{i-1}}{\chi_i - \chi_{i-1}} & \text{for } x \in [\chi_{i-1}, \chi_i), \\ \frac{\chi_{i+1} - x}{\chi_{i+1} - \chi_i} & \text{for } x \in [\chi_i, \chi_{i+1}), \\ 0 & \text{elsewhere,} \end{cases} \tag{37}$$

where  $\chi$  is the vector of knot points. In 2D cases, the contact region is a segment, and the necessary  $n_x$  B-Spline basis functions are defined over  $n_x + 2$  knots points,  $\chi = \{\chi_0, \dots, \chi_{n_x+1}\}$ . The knots are chosen to span the contact segment with some margin. Now, the normal traction profile can be defined as

$$t_N(\tilde{X}; \phi_c) = \sum_{i=1}^{n_x} B^i(\tilde{X}_x, \chi) \cdot \phi_c^i, \tag{38}$$

which allows to recover the parametrized traction field

$$t_c(\tilde{X}; \phi_c) = \{0, t_N(\tilde{X}; \phi_c)\} \tag{39}$$

that is necessary for Eq. (30). In 3D cases, the contact traction is parametrized over a rectangular contact zone that is specified by two vectors of knot points,  $\chi = \{\chi_0, \dots, \chi_{n_x+1}\}$  and  $\zeta = \{\zeta_0, \dots, \zeta_{n_y+1}\}$ , and the product of two B-Spline bases,  $B^i(x, \chi) \cdot B^j(y, \zeta)$ , is used. The parametrized normal traction and traction vector read

$$t_N(\tilde{X}; \phi_c) = \sum_{i=1}^{n_x} \sum_{j=1}^{n_y} B^i(\tilde{X}_x, \chi) B^j(\tilde{X}_y, \zeta) \cdot \phi_c^{i,j}, \tag{40}$$

$$t_c(\tilde{X}; \phi_c) = \{0, 0, t_N(\tilde{X}; \phi_c)\}. \tag{41}$$

Note, that in 3D cases the vector of parameters  $\phi_c$  is of length  $n_x \cdot n_y$ .

**Remark.** As stated in the introduction, we limit ourselves to path-independent problems, which excludes the frictional contact. Although we can see no technical obstacles to introduce friction (tangential contact traction) into the inverse- and forward elasticity parts of the proposed optimization framework, we have concerns about the uniqueness of solution if the friction is present. To this end, we leave this question for future research.

### 3.3. Sensitivity analysis

The gradient of design functional with respect to design parameters (which is necessary for gradient-based minimization algorithms) involves the gradient of the solution expressed by Eq. (35). This gradient is expressed *implicitly* through the solution of inverse-forward elasticity problems given by Eqs. (31) and (32). To recover this implicit gradient, in this work we use the direct differentiation method of sensitivity analysis, see Michaleris et al. [46]. The method utilizes discretized residual forms given by Eqs. (19) and (27), of the forward and inverse elasticity problems, respectively. Knowing that

$$\mathbb{R}(\mathfrak{u}(\boldsymbol{\phi}), \mathbb{X}(\boldsymbol{\phi}), \boldsymbol{\phi}) \equiv \mathbf{0} \quad \text{and} \quad \tilde{\mathbb{R}}(\tilde{\mathfrak{u}}(\boldsymbol{\phi}), \boldsymbol{\phi}) \equiv \mathbf{0} \quad (42)$$

hold for all  $\boldsymbol{\phi}$  (through their solution for  $\mathfrak{u}$  and  $\tilde{\mathfrak{u}}$ ), we can obtain the necessary gradients as a solution of two sets of *linear* equations

$$\nabla_{\phi_i} \mathfrak{u} = -\mathbb{K}^{-1} \cdot \left( \frac{\partial \mathbb{R}}{\partial \phi_i} + \frac{\partial \mathbb{R}}{\partial \mathbb{X}} \cdot \nabla_{\phi_i} \tilde{\mathfrak{u}} \right) \quad (43)$$

$$\nabla_{\phi_i} \tilde{\mathfrak{u}} = -\tilde{\mathbb{K}}^{-1} \cdot \frac{\partial \tilde{\mathbb{R}}}{\partial \phi_i}. \quad (44)$$

The right-hand sides of the linear problems solved above are called sensitivity pseudo-loads. Eq. (43) involves the velocity field of shape sensitivity,  $\nabla_{\phi_i} \tilde{\mathfrak{u}}$ , which is given through the solution of Eq. (44). Quite notably, the linear operators  $\mathbb{K} = D\mathbb{R}/D\mathfrak{u}$  and  $\tilde{\mathbb{K}} = d\tilde{\mathbb{R}}/d\tilde{\mathfrak{u}}$  are the same consistent stiffness matrices that are used at the last iterations of the Newton–Raphson method when solving Eqs. (19) and (27), respectively. The technique is thus able to provide numerical-precision sensitivities, and it only requires solving two systems of linear equations per gradient  $\nabla_{\phi_i} \mathfrak{x}$ .

**Remark.** The most straightforward method to achieving implicit gradients is to apply the finite difference scheme (center differences)

$$\nabla_{\phi_i} \mathfrak{x} = \frac{d\mathfrak{x}}{d\phi_i} \approx \frac{\mathfrak{x}(\boldsymbol{\phi} + \Delta_i \boldsymbol{\phi}) - \mathfrak{x}(\boldsymbol{\phi} - \Delta_i \boldsymbol{\phi})}{2\|\Delta_i \boldsymbol{\phi}\|}, \quad (45)$$

where  $\Delta_i \boldsymbol{\phi}$  is the perturbation in the direction of the  $i$ th component of  $\boldsymbol{\phi}$ . This method is inefficient for a larger number of parameters because it requires two executions of the whole inverse-forward problem per gradient  $\nabla_{\phi_i} \mathfrak{x}$ . It has been, however, used in the present work to validate the gradients computed with the direct differentiation method of sensitivity analysis.

## 4. Results

Three benchmark examples will be presented to verify the implementation of the framework and to demonstrate its capabilities. In the benchmark examples we also analyze the influence of noise, which provides a basic assessment of applicability the framework to work with real experimental data. In all the examples, the deformed configurations are only loaded in by their masses in the gravitational field (no Neumann BCs are present, except the contact traction). We imitated the rotation of the sample by changing the direction of gravity. In Section 4.1, we performed a basic verification of the inverse elasticity formulation and of the sensitivity analysis for all three benchmark examples. In Section 4.2, the identification of material parameters of a two-phase soft material is demonstrated. In Section 4.3, the identification problem is extended to the case that includes frictionless contact in both loaded configurations.

The implementation of finite element procedures has been done with *AceGen/AceFem* system, see Korelc [47,48] and Wriggers and Korelc [49]. *AceGen* is an automatic-differentiation system that interprets FE formulations expressed in a Mathematica-based symbolic language, and then automatizes the derivation of computationally-efficient FE procedures. It has been used to facilitate the implementation of finite element residual vectors, see Eqs. (19) and (27), their linearization, as well as the sensitivity pseudo-load vectors used in Eqs. (43)–(44).

The benchmark examples are prepared as follows. We compute necessary loaded configurations and use them as initial configurations for inverse elasticity problems or final configurations for inverse+forward elasticity problems. Thanks to that, we can compare the solutions of the inverse (inverse+forward) elasticity problem with the expected known *in silico* results.

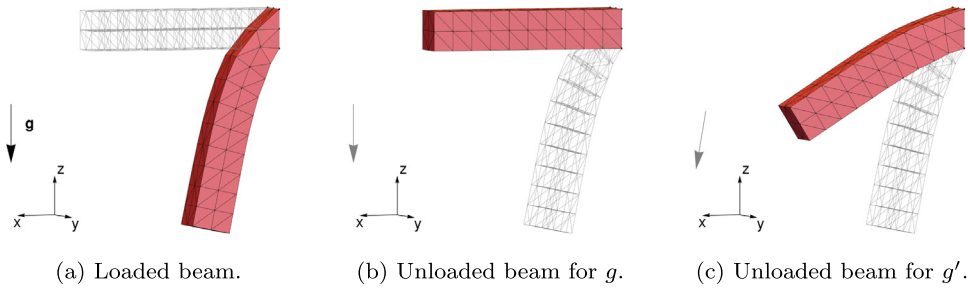


**Fig. 4.** Beam benchmark example. FE solution of (a) forward deformation and the corresponding (b) inverse deformation. (The presented case corresponds to the first row in Table 1.) The light gray arrows refer to the initial load. The gray wire-frames denote initial configurations of the respective forward- and inverse problems. Case (c) shows the solution of the inverse elasticity problem in which the gravity direction was rotated by  $10^\circ$  clockwise with respect to the one that was used to obtain the loaded (initial) configuration.



**Fig. 5.** Beam benchmark example. Sensitivity fields of the inverse elasticity problem (for the case provided in row 1 in Table 1).

#### 4.1. Validation of the inverse and inverse-forward formulation

For basic validation of the inverse elasticity formulation, we consider a  $30 \text{ cm} \times 6 \text{ cm} \times 6 \text{ cm}$  beam that is clamped on the left side and subjected to gravity loading (see Fig. 4(a)). The discretized FE model of the beam consists of 240 first-order tetrahedral elements (O1). (Note that other element types/topologies are also compatible with the proposed method. To demonstrate this, the second order tetrahedral (O2) mesh and the first order hexahedral (H1) mesh were also included in the benchmark.) The neo-Hookean material model is assumed (see Eq. (4)), and the material parameters are chosen such that the beam undergoes large deformation.

In Fig. 4 we can see the solution to the inverse elasticity problem. Even though the initial configuration was highly deformed, the original unloaded shape could be successfully retrieved. This was only possible because the formulation and its implementation were correct, and because we provided exact material parameters and loading conditions (i.e., the ones that were used to compute the initial loaded configuration shown in Fig. 4(a)). Indeed, if a different direction of gravity from the forward step one is chosen for the inverse problem, the solution of the inverse elasticity problem is not matching the initial unloaded configuration anymore, see Fig. 4(c).

In Fig. 5 we provide the solution to the sensitivity problem for the inverse elasticity formulation of  $E$  and  $\rho$ . We can observe a high correlation of those sensitivity fields, with  $\|E \cdot \nabla_E \tilde{u} + \rho \cdot \nabla_\rho \tilde{u}\| \simeq 10^{-14}$ . This correlation is an effect of linear dependency of the elastic strain energy potential on Young's modulus (see Eq. (4)), and lack of Neumann boundary conditions (only body forces are present). For these two reasons, when neglecting the boundary terms in the weak forms (7) and (11), a single independent parameter  $E/\rho$  can be extracted, and the solution only depends on that ratio, making the two parameters correlated. As a consequence,

$$E \cdot \nabla_E \tilde{u} \approx -\rho \cdot \nabla_\rho \tilde{u}, \tag{46}$$

holds (up to machine precision), and one cannot simultaneously identify  $E$  and  $\rho$  as independent parameters. This fact is utilized later in the present paper in the optimization examples, for which we keep the density fixed to allow for unique identification of the elastic modulus.

We performed a thorough validation campaign for the inverse- and inverse-forward elasticity problems, as well as for the respective sensitivity problems. The error metrics used in the validation are the following. The solution

**Table 1**

Validation and performance study of the inverse elasticity problem for the beam geometry. Different values of material parameters and the gravity vector are checked. The fourth and fifth columns provide the number of necessary load increment steps (and the total number of Newton–Raphson (N–R) iterations) needed by the solver for the case of forward (F) and inverse (I) problems, respectively. Error metrics for the displacement and the sensitivities are provided in columns 6th and 7th, respectively.

$(E$ [Pa], $\nu$ [ ], $\rho$ [kg m <sup>-3</sup> ])	$(g_x, g_y, g_z)$ [N m <sup>-3</sup> ]	Topology	F steps (N–R iter.)	I steps (N–R iter.)	$\varepsilon_{\mathbf{x}}$	$\varepsilon_{\mathbf{x}}^{\text{sens}}$
$(10^3, 0.45, 50)$	$(0., 0., -9.81)$	O1	5 (41)	1 (9)	$3.9 \cdot 10^{-16}$	$1.6 \cdot 10^{-9}$
<b><math>(10^4, 0.45, 50)</math></b>	$(0., 0., -9.81)$	O1	1 (7)	1 (5)	$4.2 \cdot 10^{-16}$	$1.4 \cdot 10^{-9}$
$(10^3, \mathbf{0.20}, 50)$	$(0., 0., -9.81)$	O1	4 (31)	1 (7)	$3.1 \cdot 10^{-16}$	$6.1 \cdot 10^{-10}$
$(10^3, 0.45, \mathbf{20})$	$(0., 0., -9.81)$	O1	2 (22)	1 (7)	$4.5 \cdot 10^{-16}$	$1.6 \cdot 10^{-9}$
$(10^3, 0.45, 50)$	$(0., \mathbf{-5.7, -8})$	O1	6 (47)	1 (9)	$1.9 \cdot 10^{-16}$	$1.9 \cdot 10^{-9}$
$(10^3, 0.45, 50)$	$(0., 0., -9.81)$	<b>O2</b>	9 (71)	1 (9)	$8.42 \cdot 10^{-16}$	$1.2 \cdot 10^{-9}$
$(10^3, 0.45, 50)$	$(0., 0., -9.81)$	<b>H1</b>	8 (71)	1 (9)	$5.0 \cdot 10^{-16}$	$2.7 \cdot 10^{-9}$

$\mathbb{X}$  is compared against the known expected solution  $\mathbb{X}^*$  using the relative error

$$\varepsilon_{\mathbf{x}} = \|\mathbb{X} - \mathbb{X}^*\| / \|\mathbb{X}^*\|. \quad (47)$$

The sensitivities of the solution are cross-validated by checking the relative error

$$\varepsilon_{\mathbf{x}}^{\text{sens}} = \max_i \left( \frac{\|\text{DDM}(\nabla_{\phi_i} \tilde{\mathbf{u}}) - \text{FD}(\nabla_{\phi_i} \tilde{\mathbf{u}})\|}{\|\text{FD}(\nabla_{\phi_i} \tilde{\mathbf{u}})\|} \right), \quad (48)$$

in which  $\text{DDM}(\cdot)$  are sensitivities computed with the direct differentiation method given by Eq. (44) and  $\text{FD}(\cdot)$  are respective finite-difference approximations provided by Eq. (45). The above-mentioned metrics of the inverse elasticity solutions naturally extend to the respective inverse-forward cases, in which we have the error metrics  $\varepsilon_{\mathbf{x}}$  and  $\varepsilon_{\mathbf{x}}^{\text{sens}}$  that are related to the solution  $\mathbf{x} = \tilde{\mathbf{X}} + \tilde{\mathbf{u}} + \mathbf{u}$ .

For the inverse elasticity problem, the study has been done for a variety of material parameters (stiffness, compressibility, density), loading directions (bending, bending with torsion) and element topologies, which are summarized in Table 1 first three columns. The selected results for the case of inverse elasticity of the beam are provided in Table 1. The differences in the number of steps which are necessary to converge for the forward problem (column 4) for different cases are something expected. For instance, the low number of steps in line 2 and 4 results from a lower deformation (higher stiffness or lower density). On the other hand, higher numbers of necessary steps in line 5 are due to a more complex load and in lines 6 and 7 results from the use of more complex element topologies. The computed displacements are numerically exact to the known solution, and the computed sensitivities are successfully cross-validated.

We can also observe in Table 1 that, quite surprisingly, the solution procedure of the inverse elasticity problem requires less iterations (steps) than for the forward elasticity case. Our understanding of this effect is the following. Due to extreme deformations, in the forward elasticity analysis, the deformed mesh is highly distorted. This distorted mesh is an element of solution, which makes it very likely to cause divergence of the Newton–Raphson solution scheme when increasing the load too rapidly in the adaptive load-stepping procedure (i.e., the convergence radius is small). Because of that, more steps are necessary to reach the solution of the forward elasticity problem. For the inverse elasticity problem, the highly distorted mesh is fixed (the initial configuration), while the final mesh is not distorted, which makes the convergence of the Newton–Raphson scheme easier, even for large load increments (i.e., the convergence radius is large). Our hypothesis is to some extent confirmed by the cases in lines 2 and 4 in Table 1. In these cases, the deformations are much smaller (because of higher stiffness or lower density), which makes the solutions of forward- and inverse problems the same easy.

A similar performance/validation study has been done for the inverse-forward problem, for all the benchmark examples considered in this section, i.e., also including the multi-part (simplified breast geometry) case described in Section 4.2 and the tire case described in Section 4.3. Selected examples are provided in Table 2, and, again, prove the excellent performance of the inverse- and inverse-forward frameworks.

**Table 2**

Validation and performance study of the inverse-forward elasticity problem for three benchmark examples. The gravity field  $g_0$  is used in the inverse problem and the gravity field  $g$  in the subsequent forward problem (both in  $N m^{-3}$ ). The 4th and 5th columns provide the number of necessary load increment steps (and the total number of Newton–Raphson (N–R) iterations) needed by the solver for the case of inverse (I) and forward (F) problems, respectively. Error metrics for the displacement of the inverse problem and the sensitivities of the inverse- and inverse-forward problems are provided in columns 6th, 7th and 8th, respectively; Young’s modulus, Poisson ratio and density were respectively set to 1000 Pa, 0.45, 50  $kg m^{-3}$  for the beam case,  $(E_t, \nu_t, \rho_t; E_s, \nu_s, \rho_s) = (1000 Pa, 0.45, 1000 kg m^{-3}; 1000 Pa, 0.45, 1000 kg m^{-3})$  for the breast case, and 1000 Pa, 0.45, 200  $kg m^{-3}$  for the tire case.

Geometry	$(g_x, g_y, g_z)_0$	$(g_x, g_y, g_z)$	I steps (N–R iter.)	F steps (N–R iter.)	$\epsilon_X$	$\epsilon_X^{sens}$	$\epsilon_X^{sens}$
Beam	(0., 0., -9.81)	(2., 5., -2.5)	1 (9)	5 (41)	$9.26 \cdot 10^{-17}$	$1.56 \cdot 10^{-9}$	$3.60 \cdot 10^{-8}$
Breast	(0., 0., -9.81)	(2., 5., -2.5)	1 (5)	1 (8)	$2.75 \cdot 10^{-17}$	$3.80 \cdot 10^{-10}$	$6.37 \cdot 10^{-10}$
Tire	(0., -9.81, 0.)	(0., 9.81, 0.)	1 (9)	5 (31)	$7.52 \cdot 10^{-16}$	$6.83 \cdot 10^{-9}$	$2.71 \cdot 10^{-9}$

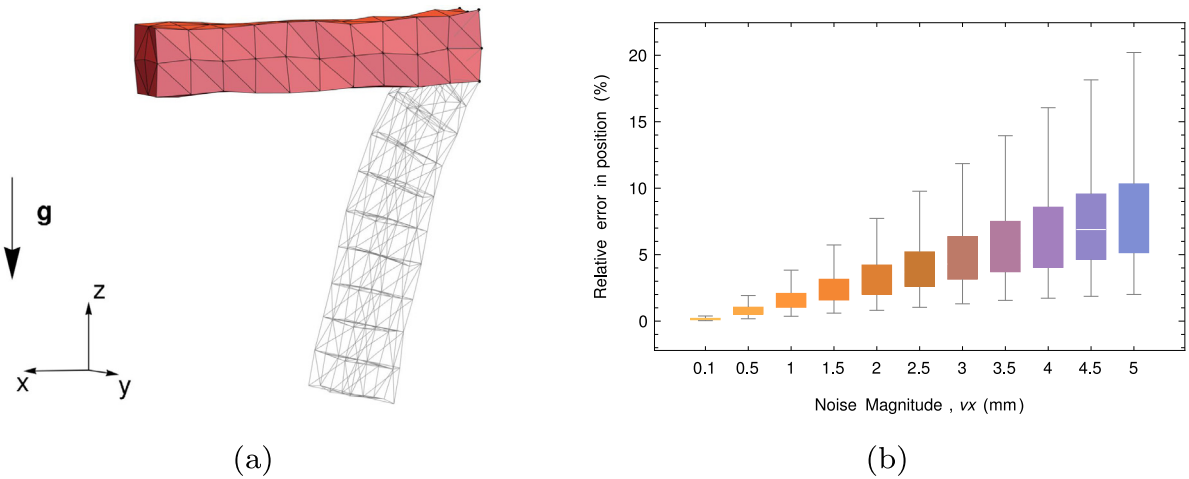


**Fig. 6.** Beam benchmark example with noise. (a) FE solution of the inverse deformation (the gray wire-frame denotes the noisy initial configuration). (b) The statistics (mean, lower & upper quartiles, min & max) of displacement relative errors (Eq. (47)) for different noise levels.

4.1.1. Effect of noise

So far, we assumed the known geometries to be perfect. They resulted from an assumed numerical model (forward elasticity), which assured the compatibility with the inverse elasticity model that was used to recover the unknown geometry and then to be a part of the calibration procedure. However, in the experimental reality we do not have perfect data. There are several sources of uncertainties/errors/noise, such as the mismatch between properties of examined material/system and an assumed model, the inaccuracies in physical imaging/measurement, or the fitting errors in the Digital Volume Correlation (DVC) procedure to achieve discretized geometries and deformation maps.

In this study, we were not aiming to investigate all possible sources of uncertainties. What we did was to add random perturbation (noise) to our perfect *in silico* geometries and see how this affects the predictions. We related the level of noise to an arbitrarily assumed voxel size, which is directly related to the accuracy/resolution of an imaging device, and can be also related to uncertainties of the DVC procedure, see our recent work Lavigne et al. [44].

In case of noisy version of the beam benchmark test (Table 1, line 1), the initial (loaded) geometry of the beam has been perturbed in the following way. A random noise  $\delta \in U[-vx, vx]$  has been individually generated and added to each nodal coordinate, where  $U[\bullet, \bullet]$  represents the uniform distribution and  $vx$  is the assumed noise level. We have tested 11 different values of noise levels,  $vx$ , in the range 0.1 mm – 5 mm.

Fig. 6(a) presents the inverse deformation solution for one chosen perturbed initial configuration for the noise level  $vx = 5$  mm. For each noise level, we have generated 100 different random perturbed geometries, which allowed us to analyze the statistics of prediction errors. The statistics is presented in Fig. 6(b), where we can observe that

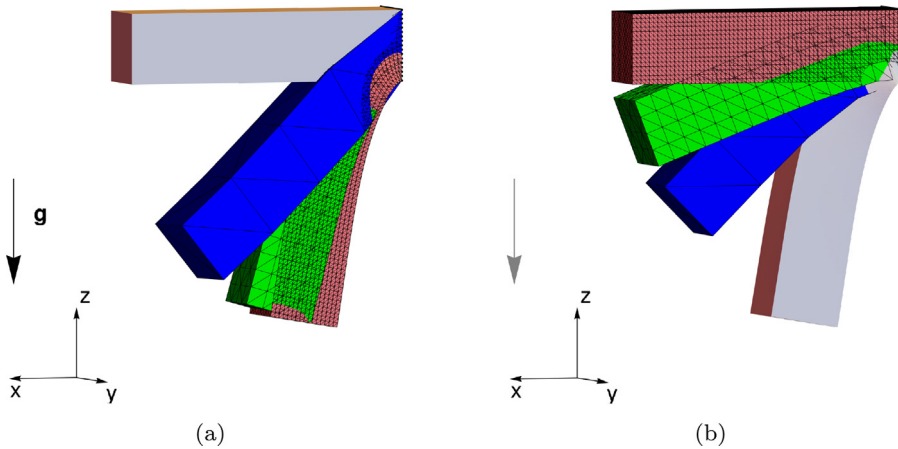


**Fig. 7.** The effect of mesh refinement on FE solutions for the (a) forward and (b) inverse elasticity problems. Different FE discretizations of the initial geometry (gray) effect in different solutions. Three mesh refinements are shown: the coarsest (blue), intermediate (green), and the finest (red). (For interpretation of the references to color in this figure legend, the reader is referred to the web version of this article.)

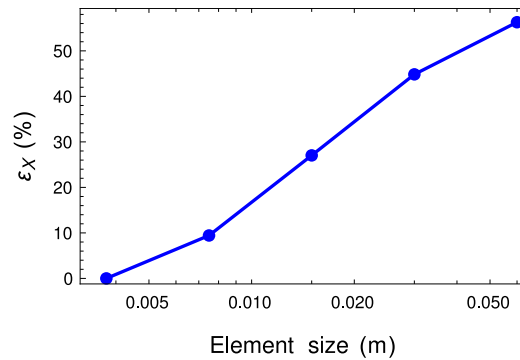


**Fig. 8.** Convergence study for the beam example. The relative error  $\epsilon_X$  (see Eq. (47)) increases with the element size (mesh coarsening).

the median and min&max values of relative error in position are proportional to the noise level. The plot shows a relatively high sensitivity of solution to noise level. This high sensitivity can be explained by extremely large deformations that are present in the studied case, as well as by the fact that the noise can significantly affect the loading conditions by changing the volume (due to body force loading).

#### 4.1.2. Convergence study

In Section 4.1.1, we showed that the solution of the inverse elasticity problem is sensitive to noise added to the initial (loaded) geometry. In this section, we will investigate the effect of coarsening or refining the finite element mesh, which can be viewed as another source of uncertainties that can affect prediction errors. To do this, we conducted the following convergence study for the beam geometry.

The study was performed for the case presented in the first row of Table 1. A reference (ground-truth) loaded configuration was calculated using the finest finite element mesh, which was made of  $6 \times n_x \times n_y \times n_z = 6 \times 2^6 \times 2^4 \times 2^4$  tetrahedrons (shown in red in Fig. 7(a)). This finest reference mesh was used to create all the coarser reference meshes for this study by gradually coarsening it by a factor of  $2 \times 2 \times 2$ . As a result, five meshes were considered:  $6 \times n_x \times n_y \times n_z = 6 \times 2^{i+2} \times 2^i \times 2^i$ ,  $i \in [0, 4]$ , all overlapping with the gray geometry in Fig. 7(b). The inverse elasticity procedure was applied to all meshes, allowing us to investigate how mesh coarsening influences the prediction error, see Fig. 7(b).

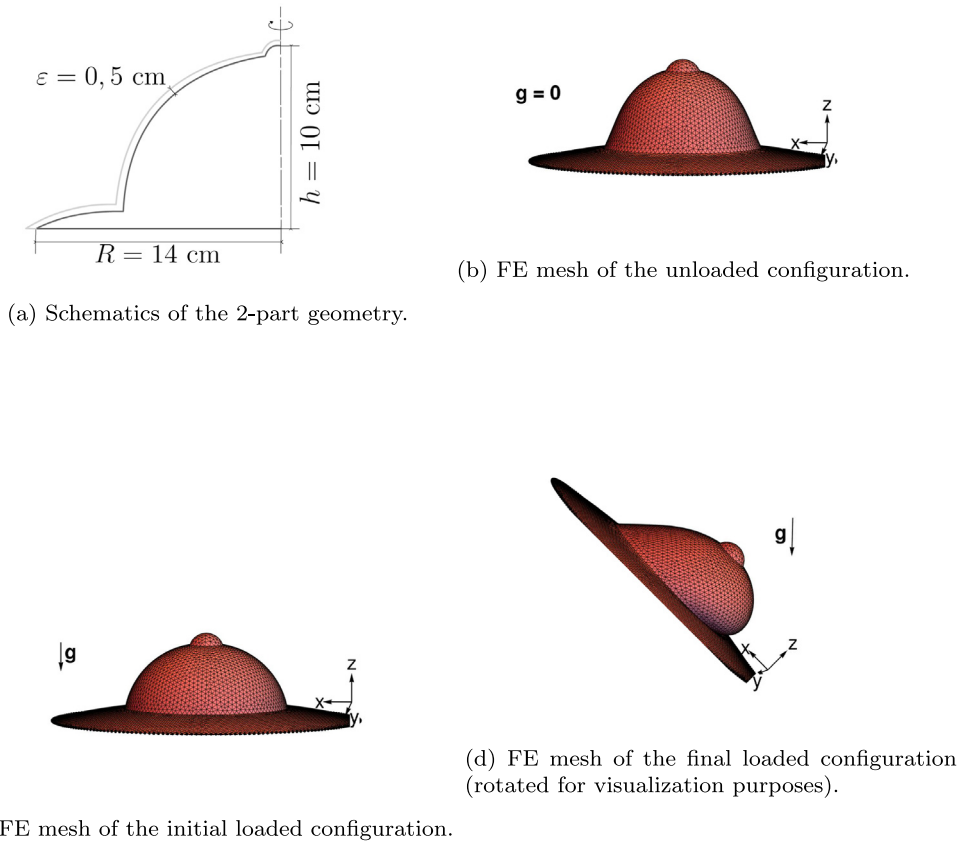


**Fig. 9.** Two-part 3D simplified breast model (tissue + skin).

In Fig. 8, we observe that the relative error is close to zero for the ground-truth mesh, but increases as the mesh is coarsened. This is expected and is primarily due to the fact that the discretized system becomes relatively stiffer as the mesh is coarsened. This is evident in the less deformed configurations obtained by solving the forward elasticity problem for coarser meshes, as shown in Fig. 7(a).

#### 4.2. Identification of material parameters

The second benchmark example is based on a simplified breast geometry. The sample consists of two parts: the body tissue and the skin, as schematically depicted in Fig. 9(a). The respective FE mesh is composed of 46 053 first-order tetrahedral elements (GMSH API was used for the meshing), see Fig. 9(b). This case aims to analyze the case of mixed stiffer/softer tissue, with a high contrast of properties. Motivated by the literature (Payan and Ohayon [1], Gamage et al. [50] and Kalra and Lowe [51]), the material parameters of the inner tissue and the skin are roughly set to  $(E_t, \nu_t, \rho_t) = (1000 \text{ Pa}, 0.45, 1000 \text{ kg m}^{-3})$  and  $(E_s, \nu_s, \rho_s) = (10\,000 \text{ Pa}, 0.45, 1100 \text{ kg m}^{-3})$ , respectively. These parameters can under-estimate the material found in the literature. The skin is usually considered incompressible. However, the chosen FE formulation only supports compressible and quasi-incompressible models. Therefore, a Poisson ratio of 0.45 was deemed a good compromise. The sample is fixed at its bottom boundary.

We will demonstrate the performance of the optimization procedure introduced in Section 3.1. The necessary initial and final deformed configurations are obtained by solving the forward elasticity problems for the gravity field  $(0, 0, -9.81) \text{ N m}^{-3}$  (initial configuration, see Fig. 9(c)) and  $(-5.7, 0, -8) \text{ N m}^{-3}$  (final configuration, see Fig. 9(d)), respectively. The four material parameters to be identified are Young's modulus and Poisson ratio of the tissue and the skin. For the reason discussed in Section 4.1, the densities were fixed. To better assess the reliability of the optimization framework, two independent identifications were performed for two different initial guesses of those

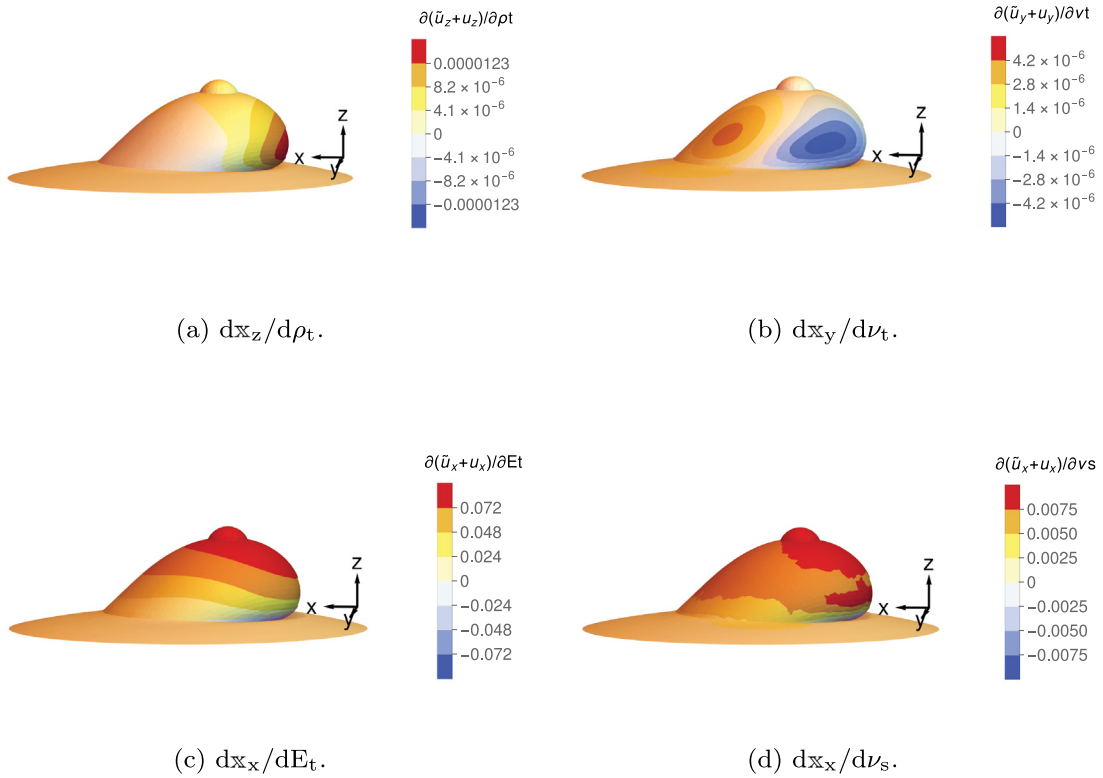


Fig. 10. Breast example. Examples of sensitivity fields of the inverse-forward elasticity problem (for the case provided in Fig. 9(d)).

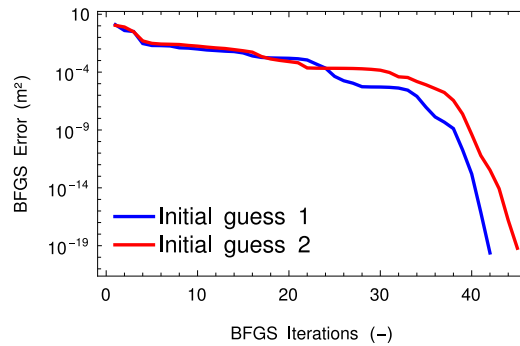


Fig. 11. Breast example. Convergence of the BFGS optimization method for two different initial guesses.

four parameters, see Table 3. The necessary gradients for the BFGS optimization method were computed with the direct differentiation method of sensitivity analysis (see exemplary sensitivity fields in Fig. 10).

The results provided in Table 3 and Fig. 11 demonstrate the excellent performance of the framework. For both initial guesses, the procedure only needed less than 50 BFGS iterations to reach the stopping criterion of  $10^{-16}$  for the square error of the solution. In both cases, the expected values of the *in silico* material parameters were found (up to numerical precision).

#### 4.2.1. Effect of noise

In Section 4.1.1 we studied the effect of noise on the solution of inverse elasticity problem. In this section, we show the effect of noise on the whole calibration procedure for the breast example. We considered three different

**Table 3**

Breast example: performance of the identification procedure. Initial guesses for the tissue and skin phases, number of required iterations for convergence (BFGS it.), and the final value of the square error (SE).

$(E_t$ [Pa], $\nu_t$ [ ], $\rho_t$ [ $\text{kg m}^{-3}$ ])	$(E_s$ [Pa], $\nu_s$ [ ], $\rho_s$ [ $\text{kg m}^{-3}$ ])	BFGS it.	SE [ $\text{m}^2$ ]
(750., 0.225, 1000)	(15000, 0.27, 1100)	41	$2.4 \cdot 10^{-20}$
(2000, 0.225, 1000)	(20000, 0.225, 1100)	44	$6.0 \cdot 10^{-20}$

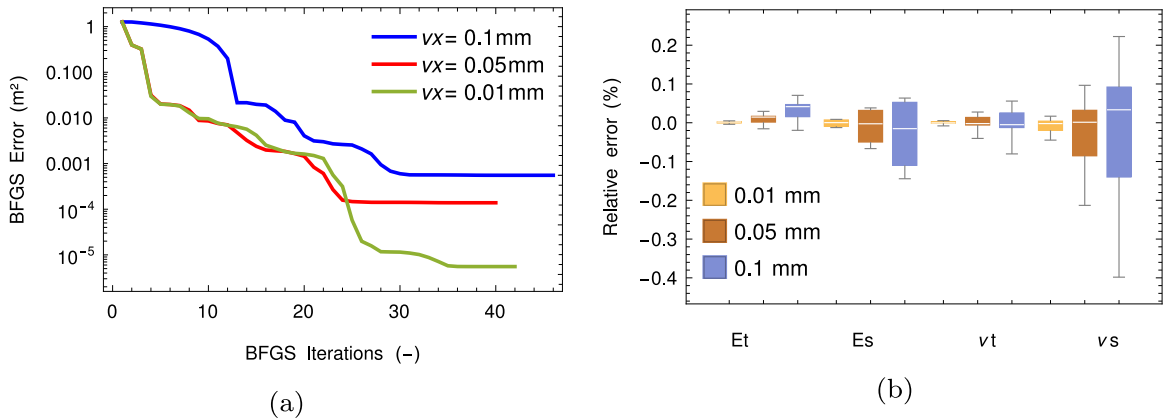


**Fig. 12.** Calibration with noise for the breast example. (a) The convergence of BFGS procedure for different noise levels. (b) The statistics (mean, lower & upper quartiles, min & max) of calibrated parameters' relative errors for different noise levels.

noise levels: 0.01 mm, 0.05 mm and 0.1 mm. The random noise was added to both known loaded geometries. The maximum noise magnitude represented 2% of the skin thickness.

For each noise level, we performed calibration for 10 different noisy cases (different random perturbations of geometries). The statistics of relative errors of identified parameters (with respect to their expected values) are summarized in Fig. 12. We can observe that, as expected, the error grows with the level of noise, however, it is lower than 0.5% for the most noisy case. We can also observe that the errors related to the parameters of skin,  $E_s$  and  $\nu_s$ , are the most affected. This can be explained by the fact that, due to its low thickness, the skin was discretized with much finer mesh, as compared to the tissue, therefore, the same level of perturbations created higher errors in strains for the skin than for the tissue, which then affected the calibration errors.

### 4.3. Identification of material parameters with contact

Finally, we will analyze the case with contact. We consider a tire-like geometry held by two semi-axes that are fixed at their free ends, see Fig. 13(a). The FE discretization consists of 43 846 first-order tetrahedral elements (created using GMSH), cf. Fig. 13(b). To obtain a large displacement field of the tire held by a stiffer axle, the material parameters of the tire are  $(E_t, \nu_t, \rho_t) = (800 \text{ Pa}, 0.4, 200 \text{ kg m}^{-3})$  and of the axles are  $(E_a, \nu_a, \rho_a) = (10^4 \text{ Pa}, 0.4, 100 \text{ kg m}^{-3})$ .

The two deformed configurations considered in this example are loaded in opposite directions, i.e.,  $\mathbf{g} = \pm(0, 9.81, 0) \text{ N m}^{-3}$ . In both loaded cases, the deformation of the sample is restricted by an obstacle located above/below (friction-less contact constraints), which results in non-trivial highly deformed configurations. The contact constraints are introduced with the penalty method. The resulting initial and final deformed shapes are shown in Figs. 13(c) and 13(d), respectively.

As a first basic test, we perform the inverse- and inverse-forward analyses in which the contact traction term in Eq. (30) is neglected ( $t_N = 0$ ). As expected, the respective solutions are incorrect, which is visible in Fig. 14. To this end, we will apply the framework introduced in Section 3.2 to identify the missing contact traction field.

The identification procedure is similar to the one presented in Section 4.2. The important difference is that, as stated in Section 3.2, we additionally parametrize the contact traction field by piece-wise bi-linear segments that are controlled by a grid of  $(n_x \times n_z)$  parameters. The grid is evenly distributed over the  $0.2 \text{ m} \times 0.2 \text{ m}$  square that

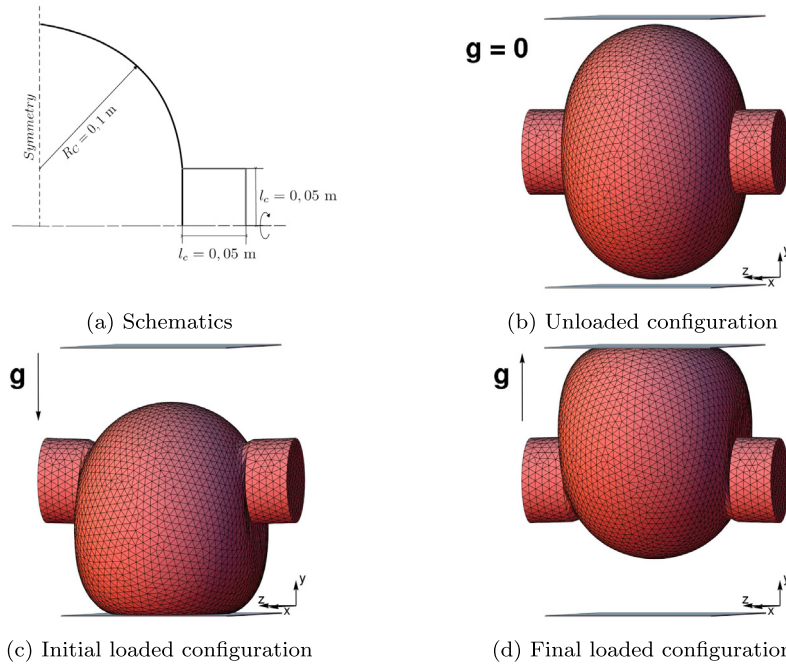


Fig. 13. Tire example. Schematics, unloaded configuration and two loaded configurations.

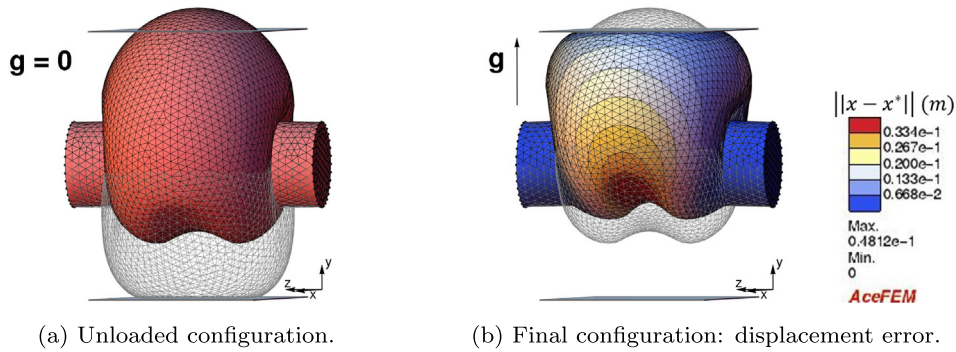
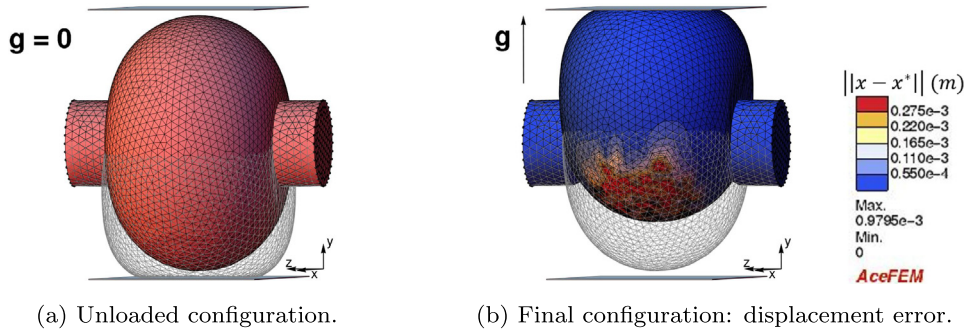


Fig. 14. Tire example for the correct material parameters but incorrect contract traction  $t_N = 0$ . The gray meshes in (a) and (b) are the reference configurations for the inverse- and forward elasticity problems, respectively.

Table 4

Tire example. The convergence study for different  $(n_x, n_z)$  resolutions. The chosen number of BFGS iterations is shown, together with the identified material parameters (Young modulus and Poisson ratio of the tire) and their relative error. BFGS error =  $\|\mathbb{x}^{\text{computed}} - \mathbb{x}^{\text{expected}}\|^2$  is the value of the minimized design functional, and MPE =  $\max \text{abs}(\mathbb{x}^{\text{computed}} - \mathbb{x}^{\text{expected}})$ , is the maximal nodal position error in the final configuration.

$(n_x, n_z)$	BFGS iterations	Solution: $(E_t$ [Pa], $\nu_t$ [ ])	Solution error (%)	BFGS error [m <sup>2</sup> ]	MPE [m]
(2, 2)	80	(761.0, 0.372)	(4.9, 7.0)	$1.29 \cdot 10^{-1}$	$1.91 \cdot 10^{-2}$
(3, 3)	120	(798.5, 0.398)	$(1.9 \cdot 10^{-1}, 5 \cdot 10^{-1})$	$2.98 \cdot 10^{-3}$	$5.91 \cdot 10^{-3}$
(4, 4)	200	(802.8, 0.401)	$(3.5 \cdot 10^{-1}, 2.5 \cdot 10^{-1})$	$1.03 \cdot 10^{-3}$	$2.34 \cdot 10^{-3}$
(6, 6)	400	(801.3, 0.400)	$(1.6 \cdot 10^{-1}, 5.3 \cdot 10^{-2})$	$3.74 \cdot 10^{-4}$	$1.84 \cdot 10^{-3}$
(8, 8)	1000	(800.1, 0.400)	$(1.5 \cdot 10^{-2}, 2.8 \cdot 10^{-3})$	$5.27 \cdot 10^{-5}$	$8.45 \cdot 10^{-4}$



**Fig. 15.** Tire example for the optimized  $8 \times 8$  case. The gray meshes in (a) and (b) are the reference configurations for the inverse- and forward elasticity problems, respectively.

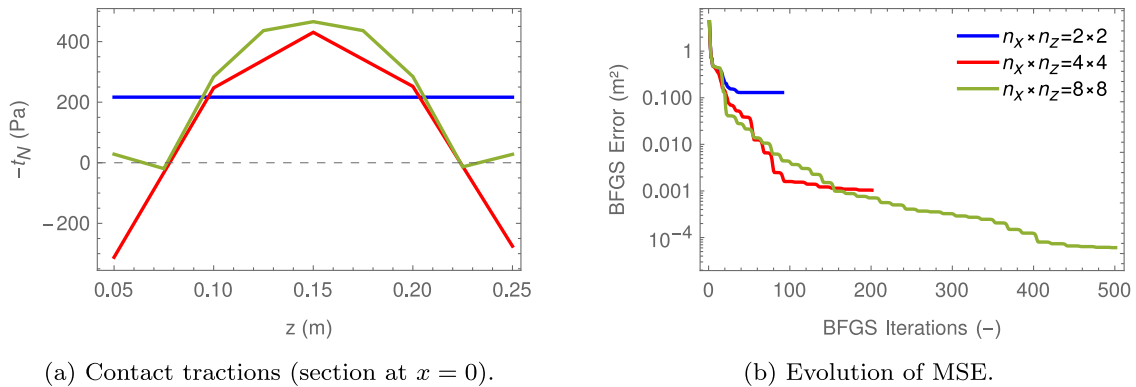


**Fig. 16.** Tire example. (a) The optimized contact traction fields, and (b) the convergence of BFGS procedure, for three different resolutions  $n_x \times n_z$ . (cropped at 500 iterations for the ease of reading).

includes the contact area of the initial loaded configuration. These contact traction parameters are identified together with two material parameters of the tire,  $(E_t, \nu_t)$ . The remaining material parameters, i.e.,  $\rho_t, E_a, \nu_a, \rho_a$ , are fixed during the identification procedure. The choice to fix  $\rho_t$  is a direct consequence of the interplay between the Young modulus and the density, discussed in Section 4.1. The parameters of stiffer axle are not upon calibration because the axle was only introduced to simulate a clamping device.

In the study, we consider a different number of contact traction parameters, starting from  $2 \times 2$  up to  $8 \times 8$ , see Table 4. This allows us to control the resolution at which the traction field can be identified: the higher the resolution is the more accurate should be the result of identification. The initial guess for the identification procedure was: random (close to zero) contact traction parameters and  $(E_t, \nu_t) = (1600 \text{ Pa}, 0.2)$ . Due to the approximate representation of the contact traction, the exact solution cannot be reached up to numerical precision (which was possible in the noiseless breast example). As a consequence, the BFGS error will reach a plateau at a finite level. The fact of reaching this plateau will be considered as our stopping criterion (different for each analyzed case), which is expressed as “BFGS iterations” in Table 4.

We can observe that the identification procedure performs very well, see Table 4 and Figs. 15–16. Even for the lowest analyzed resolution,  $n_x \times n_z = 2 \times 2$ , the identified material parameters are within 10% relative error, with the maximal position error of approx. 19 mm which is 19% of the tire radius. For the increasing resolution, the accuracy increases too, reaching the level below 0.02% relative error for material parameters and below 1 mm maximal position error for the  $8 \times 8$  resolution.

**Remark.** The increased accuracy is achieved at the cost of higher computation time. A larger number of design parameters increases both: the required number of BFGS iterations and the computational cost of each iteration

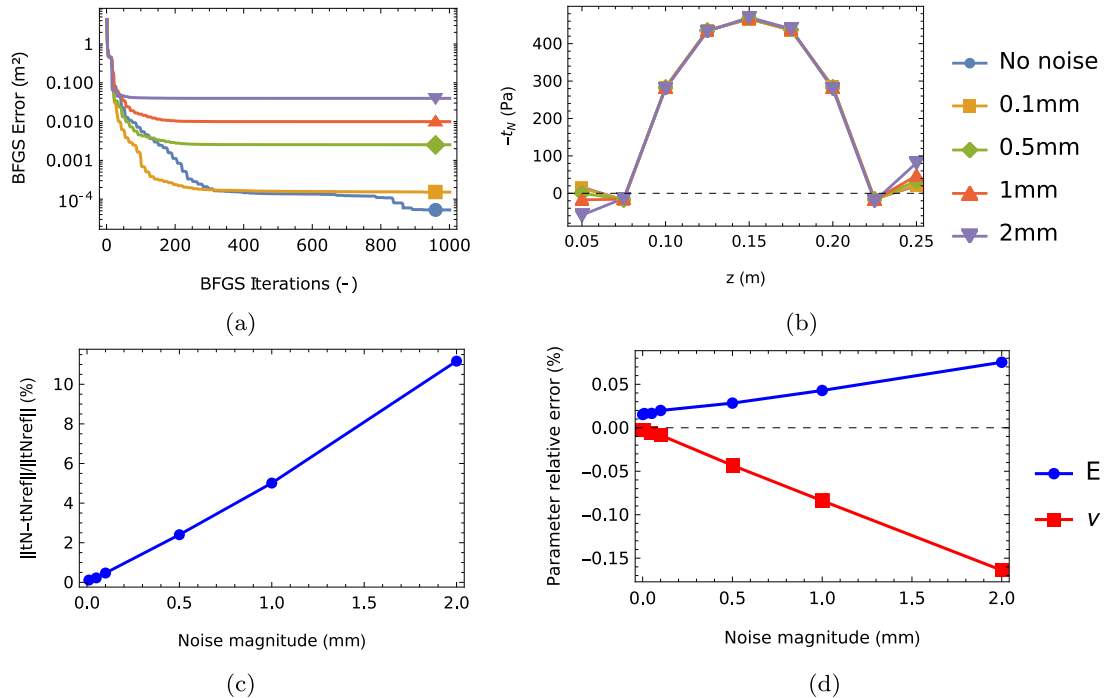


**Fig. 17.** Effect of noise on the calibration for the  $n_x \times n_z = 8 \times 8$  tire example, for different noise magnitudes. (a) Evolution of the BFGS error. (b) Contact tractions (at  $x = 0$ ). (c) Calibration errors of contact tractions (relative error with respect to the noiseless predictions). (d) Calibration errors of material parameters (relative error with respect to the exact values).

(computation of gradient). In practical applications, a suitable balance must be then found between the accuracy and the computation time.

#### 4.3.1. Effect of noise

Similarly to the breast benchmark case, we introduced noise in the tire calibration case to assess the robustness of the method (we only analyzed the case  $n_x \times n_z = 8 \times 8$ ). We considered noise levels,  $v_x$ , up to 2 mm (which is 2% of the tire radius), and used them to perturb the reference (loaded) geometries.

As expected, the BFGS error is increasing with the noise level, see Fig. 17(a). In Fig. 17(b), we can observe that the calibration error for contact tractions is pronounced the most near the boundary and outside the contact area, which correlates with the analogous results for the noiseless case shown in Fig. 16(a). This error, however, significantly influences the overall relative error for contact tractions, see Fig. 17(c), and goes above 10% for the highest analyzed noise level. Happily, the error in contact tractions does not significantly affect the calibration error for material parameters, which is below 0.2% for the highest analyzed noise level, see Fig. 17(d).

## 5. Conclusions

In this paper, we provided an optimization framework that is capable of identifying material parameters and the contact traction field, knowing only two meshes for two deformed configurations. Remarkably, both known configurations are loaded and subjected to contact with no information about contact traction. To the best of our knowledge, this is the first time such identification is shown to be possible.

In the framework, we incorporated large-deformation inverse and forward elasticity formulations, friction-less contact, as well as the parametrized unknown contact traction field that was applied as a boundary term in the inverse elasticity formulation. In the paper, we provided the details of the continuum and FE formulations, as well as the direct differentiation method of sensitivity analysis that allowed us to compute necessary gradients efficiently. In a series of numerical examples, we confirmed the correctness of the formulation and its implementation and studied

the performance of the framework, also for systems of heterogeneous material properties. Possible application of the framework to real experimental data has been demonstrated by showing its good performance when noise was artificially added to *in silico* reference geometries.

We limited ourselves to hyper-elastic material models and frictionless contact. Extension of the framework to more general models and problems (e.g., path-dependent or irreversible problems) may pose obstacles of a more fundamental (theoretical) nature. Technically, in this more general case, one could replace the efficient (direct) inverse formulation with an iterative scheme, however, this would greatly deteriorate the computational efficiency of the framework. As an alternative, an interesting avenue to investigate is to apply machine-learning techniques to retrieve computationally efficient surrogate models (see Mendizabal et al. [52], Deshpande et al. [53,54,55] and Krokos et al. [56] for the case of large-deformation elasticity), or even to extend the framework with model selection strategies, see, e.g., Thakolkaran et al. [57]. Such extensions and new directions are beyond the scope of the present paper and are left for future research.

The application area of the proposed framework is wide and covers full-field experimental model calibration procedures for natural and engineering systems that operate under load, with possible contact interactions. The unique capabilities of the framework seem particularly useful in biomedicine which must intrinsically consider soft confined systems under loads. This includes patient-specific data-driven modeling of soft human tissues, which is an emerging area of research, also pursued by our group, see Elouneq et al. [58] and Mazier et al. [59]. To this end, we believe that the presented framework will stimulate further research in that direction, and will find practical use in many engineering applications.

### Declaration of competing interest

The authors declare that they have no known competing financial interests or personal relationships that could have appeared to influence the work reported in this paper.

### Data availability

No data was used for the research described in the article.

### Acknowledgments

This study was supported by the European Union's Horizon 2020 research and innovation program under grant agreement No. 811099, the Marie Skłodowska-Curie, Luxembourg grant agreement No. 764644, and the Fonds National de la Recherche (FNR), Luxembourg Project No. C20/MS/14782078/QuaC. JL would like to acknowledge the support from EU Horizon 2020 Marie Skłodowska Curie Individual Fellowship MOrPhEM under Grant 800150.

### References

- [1] Y. Payan, J. Ohayon, *Biomechanics of Living Organs*, Academic Press, San Diego, CA, 2017, URL: <https://doi.org/10.1016/c2015-0-00832-2>.
- [2] A. Míra, A.-K. Carton, S. Muller, Y. Payan, A biomechanical breast model evaluated with respect to MRI data collected in three different positions, *Clin. Biomech.* 60 (2018) 191–199, URL: <https://doi.org/10.1016/j.clinbiomech.2018.10.020>.
- [3] A. Míra, Y. Payan, A.-K. Carton, P.M. de Carvalho, Z. Li, V. Devauges, S. Muller, Simulation of breast compression using a new biomechanical model, in: J.Y. Lo, T.G. Schmidt, G.-H. Chen (Eds.), *Medical Imaging 2018: Physics of Medical Imaging*, Vol. 10573, International Society for Optics and Photonics, SPIE, 2018, pp. 1349–1357, URL: <https://doi.org/10.1117/12.2293488>.
- [4] A. Míra, A.-K. Carton, S. Muller, Y. Payan, Breast biomechanical modeling for compression optimization in digital breast tomosynthesis, in: A. Gefen, D. Weihs (Eds.), *Computer Methods in Biomechanics and Biomedical Engineering*, Springer International Publishing, Cham, 2018, pp. 29–35, URL: [https://doi.org/10.1007/978-3-319-59764-5\\_4](https://doi.org/10.1007/978-3-319-59764-5_4).
- [5] P.R. Bakic, M. Albert, D. Brzakovic, A.D.A. Maidment, Mammogram synthesis using a 3D simulation. I. Breast tissue model and image acquisition simulation, *Med. Phys.* 29 (9) (2002) 2131–2139, URL: <https://doi.org/10.1118/1.1501143>.
- [6] T.-C. Shih, J.-H. Chen, D. Liu, K. Nie, L. Sun, M. Lin, D. Chang, O. Nalcioğlu, M.-Y. Su, Computational simulation of breast compression based on segmented breast and fibroglandular tissues on magnetic resonance images, *Phys. Med. Biol.* 55 (14) (2010) 4153–4168, URL: <https://doi.org/10.1088/0031-9155/55/14/013>.
- [7] A. Bilger, *Patient-Specific Biomechanical Simulation for Deep Brain Stimulation (Theses)*, Université des Sciences et Technologie de Lille, 2014, URL: <https://hal.inria.fr/tel-01097488>.
- [8] M.L. Raghavan, B. Ma, M.F. Fillingner, Non-invasive determination of zero-pressure geometry of arterial aneurysms, *Ann. Biomed. Eng.* 34 (9) (2006) 1414–1419, URL: <https://doi.org/10.1007/s10439-006-9115-7>.

- [9] J. Lu, X. Zhou, M.L. Raghavan, Inverse elastostatic stress analysis in pre-deformed biological structures: Demonstration using abdominal aortic aneurysms, *J. Biomech.* 40 (3) (2007) 693–696, URL: <https://doi.org/10.1016/j.jbiomech.2006.01.015>.
- [10] X. Zhou, J. Lu, Estimation of vascular open configuration using finite element inverse elastostatic method, *Eng. Comput.* 25 (1) (2008) 49–59, URL: <https://doi.org/10.1007/s00366-008-0104-3>.
- [11] M.M. Dooley, Model-based elastography: a survey of approaches to the inverse elasticity problem, *Phys. Med. Biol.* 57 (3) (2012) R35.
- [12] B. Eiben, V. Vavourakis, J.H. Hipwell, S. Kabus, C. Lorenz, T. Buelow, D.J. Hawkes, Breast deformation modelling: comparison of methods to obtain a patient specific unloaded configuration, in: Z.R. Yaniv, D.R. Holmes (Eds.), *SPIE Proceedings*, SPIE, 2014, URL: <https://doi.org/10.1117/12.2043607>.
- [13] B. Eiben, L. Han, J. Hipwell, T. Mertzaniidou, S. Kabus, T. Buelow, C. Lorenz, G. Newstead, H. Abe, M. Keshtgar, S. Ourselin, D. Hawkes, Biomechanically guided prone-to-supine image registration of breast MRI using an estimated reference state, in: *2013 IEEE 10th International Symposium on Biomedical Imaging*, IEEE, 2013, URL: <https://doi.org/10.1109/isbi.2013.6556450>.
- [14] T. Carter, C. Tanner, N. Beechey-Newman, D. Barratt, D. Hawkes, MR navigated breast surgery: Method and initial clinical experience, in: D. Metaxas, L. Axel, G. Fichtinger, G. Székely (Eds.), *Medical Image Computing and Computer-Assisted Intervention – MICCAI 2008*, Springer Berlin Heidelberg, Berlin, Heidelberg, 2008, pp. 356–363, URL: [https://doi.org/10.1007/978-3-540-85990-1\\_43](https://doi.org/10.1007/978-3-540-85990-1_43).
- [15] M.W. Gee, C. Förster, W.A. Wall, A computational strategy for prestressing patient-specific biomechanical problems under finite deformation, *Int. J. Numer. Methods Biomed. Eng.* 26 (1) (2010) 52–72, URL: <https://doi.org/10.1002/cnm.1236>.
- [16] H. Weisbecker, D.M. Pierce, G.A. Holzappel, A generalized prestressing algorithm for finite element simulations of preloaded geometries with application to the aorta, *Int. J. Numer. Methods Biomed. Eng.* 30 (9) (2014) 857–872, URL: <https://doi.org/10.1002/cnm.2632>.
- [17] P. Landkammer, M. Caspari, P. Steinmann, Improvements on a non-invasive, parameter-free approach to inverse form finding, *Comput. Mech.* 61 (4) (2017) 433–447, URL: <https://doi.org/10.1007/s00466-017-1468-2>.
- [18] M. Sellier, An iterative method for the inverse elasto-static problem, *J. Fluids Struct.* 27 (8) (2011) 1461–1470, URL: <https://doi.org/10.1016/j.jfluidstruct.2011.08.002>.
- [19] J. Bols, J. Degroote, B. Trachet, B. Verhegghie, P. Segers, J. Vierendeels, A computational method to assess the in vivo stresses and unloaded configuration of patient-specific blood vessels, *J. Comput. Appl. Math.* 246 (2013) 10–17, URL: <https://doi.org/10.1016/j.cam.2012.10.034>.
- [20] S. Govindjee, P.A. Mihalic, Computational methods for inverse finite elastostatics, *Comput. Methods Appl. Mech. Engrg.* 136 (1–2) (1996) 47–57, URL: [https://doi.org/10.1016/0045-7825\(96\)01045-6](https://doi.org/10.1016/0045-7825(96)01045-6).
- [21] A. Mazier, A. Bilger, A.E. Forte, I. Peterlik, J.S. Hale, S.P.A. Bordas, Inverse deformation analysis: an experimental and numerical assessment using the FEniCS Project, *Eng. Comput.* (2022) URL: <https://doi.org/10.1007/s00366-021-01597-z>.
- [22] V. Rajagopal, J.-H. Chung, D. Bullivant, P.M.F. Nielsen, M.P. Nash, Determining the finite elasticity reference state from a loaded configuration, *Internat. J. Numer. Methods Engrg.* 72 (12) (2007) 1434–1451, URL: <https://doi.org/10.1002/nme.2045>.
- [23] M. Kuhlmann, E.C. Fear, A. Ramirez-Serrano, S. Federico, Mechanical model of the breast for the prediction of deformation during imaging, *Med. Eng. Phys.* 35 (4) (2013) 470–478, URL: <https://doi.org/10.1016/j.medengphy.2012.06.012>.
- [24] S. Avril, M. Bonnet, A.-S. Bretelle, M. Grédiac, F. Hild, P. Jenny, F. Latourte, D. Lemosse, S. Pagano, E. Pagnacco, et al., Overview of identification methods of mechanical parameters based on full-field measurements, *Exp. Mech.* 48 (4) (2008) 381–402.
- [25] S. Goenezen, P. Barbone, A.A. Oberai, Solution of the nonlinear elasticity imaging inverse problem: The incompressible case, *Comput. Methods Appl. Mech. Engrg.* 200 (13–16) (2011) 1406–1420, <http://dx.doi.org/10.1016/j.cma.2010.12.018>.
- [26] F. Pierron, M. Grédiac, *The Virtual Fields Method: Extracting Constitutive Mechanical Parameters from Full-Field Deformation Measurements*, Springer Science & Business Media, 2012.
- [27] P.E. Barbone, A.A. Oberai, J.C. Bamber, G.P. Berry, J.-F. Dord, E.R. Ferreira, S. Goenezen, T.J. Hall, Nonlinear and poroelastic biomechanical imaging: Elastography beyond Young’s modulus, in: *Handbook of Imaging in Biological Mechanics*, Taylor and Francis, CRC Press, 2014.
- [28] F. Hild, A. Bouterf, L. Chamoin, H. Leclerc, F. Mathieu, J. Nèggers, F. Pled, Z. Tomičević, S. Roux, Toward 4D mechanical correlation, *Adv. Model. Simul. Eng. Sci.* 3 (1) (2016) 1–26.
- [29] B. Pan, Digital image correlation for surface deformation measurement: historical developments, recent advances and future goals, *Meas. Sci. Technol.* 29 (8) (2018) 082001.
- [30] F. Pierron, M. Grédiac, Towards Material Testing 2.0. A review of test design for identification of constitutive parameters from full-field measurements, *Strain* 57 (1) (2021) e12370.
- [31] B. Borzeshkowsky, I. Lubowiecka, R.A. Sauer, Nonlinear material identification of heterogeneous isogeometric Kirchhoff–Love shells, *Comput. Methods Appl. Mech. Engrg.* 390 (2022) 114442.
- [32] S. Stupkiewicz, J. Lengiewicz, J. Korelc, Sensitivity analysis for frictional contact problems in the augmented Lagrangian formulation, *Comput. Methods Appl. Mech. Engrg.* 199 (33–36) (2010) 2165–2176, URL: <https://doi.org/10.1016/j.cma.2010.03.021>.
- [33] P. Beremlijski, J. Haslinger, M. Kocvara, J. Outrata, Shape optimization in contact problems with Coulomb friction, *SIAM J. Optim.* 13 (2) (2002) 561–587, URL: <https://doi.org/10.1137/S1052623401395061>.
- [34] D. Hilding, B. Torstenfelt, A. Klarbring, A computational methodology for shape optimization of structures in frictionless contact, *Comput. Methods Appl. Mech. Engrg.* 190 (31) (2001) 4043–4060, URL: [https://doi.org/10.1016/S0045-7825\(00\)00310-8](https://doi.org/10.1016/S0045-7825(00)00310-8).
- [35] D. Song, D.T. Seidl, A.A. Oberai, Three-dimensional traction microscopy accounting for cell-induced matrix degradation, *Comput. Methods Appl. Mech. Engrg.* 364 (2020) 112935, URL: <https://doi.org/10.1016/j.cma.2020.112935>.
- [36] J. Simo, R. Taylor, Penalty function formulations for incompressible nonlinear elastostatics, *Comput. Methods Appl. Mech. Engrg.* 35 (1) (1982) 107–118.
- [37] S. Doll, K. Schweizerhof, On the development of volumetric strain energy functions, *J. Appl. Mech.* 67 (1) (2000) 17–21.

- [38] R.W. Ogden, *Non-Linear Elastic Deformations*, Dover Publications, 2005.
- [39] T.A. Laursen, *Computational Contact and Impact Mechanics*, Springer Berlin Heidelberg, 2003, URL: <https://doi.org/10.1007/978-3-662-04864-1>.
- [40] P. Wriggers, *Computational Contact Mechanics*, Springer Berlin Heidelberg, 2006, URL: <https://doi.org/10.1007/978-3-540-32609-0>.
- [41] J. Lengiewicz, J. Korelc, S. Stupkiewicz, Automation of finite element formulations for large deformation contact problems, *Internat. J. Numer. Methods Engrg.* 85 (10) (2011) 1252–1279, URL: <https://doi.org/10.1002/nme.3009>.
- [42] A. Buljac, C. Jailin, A. Mendoza, J. Neggiers, T. Taillandier-Thomas, A. Bouterf, B. Smaniotto, F. Hild, S. Roux, Digital volume correlation: Review of progress and challenges, *Exp. Mech.* 58 (5) (2018) 661–708, URL: <https://doi.org/10.1007/s11340-018-0390-7>.
- [43] P. Auger, T. Lavigne, B. Smaniotto, M. Spagnuolo, F. dell’Isola, F. Hild, Poynting effects in pantographic metamaterial captured via multiscale DVC, *J. Strain Anal. Eng. Des.* 56 (7) (2020) 462–477, URL: <https://doi.org/10.1177/0309324720976625>.
- [44] T. Lavigne, A. Mazier, A. Perney, S. Bordas, F. Hild, J. Lengiewicz, Digital Volume Correlation for large deformations of soft tissues: Pipeline and proof of concept for the application to breast ex vivo deformations, *J. Mech. Behav. Biomed. Mater.* 136 (2022) 105490, URL: <https://doi.org/10.1016/j.jmbbm.2022.105490>.
- [45] J. Nocedal, S. Wright, *Numerical Optimization*, Springer, New York, 2006, URL: <https://doi.org/10.1007/978-0-387-40065-5>.
- [46] P. Michaleris, D. Tortorelli, C. Vidal, Tangent operators and design sensitivity formulations for transient non-linear coupled problems with applications to elastoplasticity, *Internat. J. Numer. Methods Engrg.* 37 (14) (1994) 2471–2499, URL: <https://doi.org/10.1002/nme.1620371408>.
- [47] J. Korelc, AceGen/AceFEM website and user manuals, 2022, URL: <http://symbtech.fgg.uni-lj.si/>.
- [48] J. Korelc, Automation of primal and sensitivity analysis of transient coupled problems, *Comput. Mech.* 44 (5) (2009) 631–649, URL: <https://doi.org/10.1007/s00466-009-0395-2>.
- [49] P. Wriggers, J. Korelc, *Automation of Finite Element Methods*, first ed., Springer International Publishing, Cham, Switzerland, 2016.
- [50] T.P.B. Gamage, P.M. Nielsen, M.P. Nash, *Clinical Applications of Breast Biomechanics*, Elsevier, 2017, pp. 215–242, URL: <https://doi.org/10.1016/b978-0-12-804009-6.00010-9>.
- [51] A. Kalra, A. Lowe, Mechanical behaviour of skin: A review, *J. Mater. Sci. Eng.* 5 (4) (2016) URL: <https://doi.org/10.4172/2169-0022.1000254>.
- [52] A. Mendizabal, P. Márquez-Neila, S. Cotin, Simulation of hyperelastic materials in real-time using deep learning, *Med. Image Anal.* 59 (2020) 101569, URL: <https://doi.org/10.1016/j.media.2019.101569>.
- [53] S. Deshpande, J. Lengiewicz, S.P. Bordas, Probabilistic deep learning for real-time large deformation simulations, *Comput. Methods Appl. Mech. Engrg.* 398 (2022) 115307, URL: <https://doi.org/10.1016/j.cma.2022.115307>.
- [54] S. Deshpande, J. Lengiewicz, S.P.A. Bordas, MAgNET: A graph U-Net architecture for mesh-based simulations, 2022, arXiv preprint. URL: <https://doi.org/10.48550/arxiv.2211.00713>.
- [55] S. Deshpande, R.I. Sosa, S.P.A. Bordas, J. Lengiewicz, Convolution, aggregation and attention based deep neural networks for accelerating simulations in mechanics, 2022, arXiv preprint. URL: <https://arxiv.org/abs/2212.01386>.
- [56] V. Krokos, V.B. Xuan, S.P.A. Bordas, P. Young, P. Kerfriden, A Bayesian multiscale CNN framework to predict local stress fields in structures with microscale features, *Comput. Mech.* 69 (3) (2021) 733–766, URL: <https://doi.org/10.1007/s00466-021-02112-3>.
- [57] P. Thakolkaran, A. Joshi, Y. Zheng, M. Flaschel, L. De Lorenzis, S. Kumar, NN-EUCLID: deep-learning hyperelasticity without stress data, 2022, arXiv preprint [arXiv:2205.06664](https://arxiv.org/abs/2205.06664).
- [58] A. Elouneq, D. Sutula, J. Chambert, A. Lejeune, S. Bordas, E. Jacquet, An open-source FEniCS-based framework for hyperelastic parameter estimation from noisy full-field data: Application to heterogeneous soft tissues, *Comput. Struct.* 255 (2021) 106620, URL: <https://doi.org/10.1016/j.compstruc.2021.106620>.
- [59] A. Mazier, S. Ribes, B. Gilles, S.P. Bordas, A rigged model of the breast for preoperative surgical planning, *J. Biomech.* 128 (2021) 110645, URL: <https://doi.org/10.1016/j.jbiomech.2021.110645>.